

1 **Evaluation and enhancement of permafrost modeling with**
2 **the NASA Catchment Land Surface Model**

3

4 Jing Tao¹, Rolf H. Reichle², Randal D. Koster², Barton A. Forman³, Yuan Xue³

5

6 1 - Earth System Science Interdisciplinary Center, University of Maryland, College Park,
7 Maryland

8 2 - Global Modeling and Assimilation Office, NASA Goddard Space Flight Center, Greenbelt,
9 Maryland

10 3 - Department of Civil and Environmental Engineering, University of Maryland, College Park,
11 Maryland

12

13 **Correspondence to:**

14 Dr. Jing Tao (JingTao@umd.edu)

15

16 Key Points

- Profile-average RMSE of simulated soil temperature versus in situ observations is reduced by using corrected local forcing and land cover
- Subsurface heat transport is mostly realistic; when not; it is improved via treatment of soil organic carbon-related thermal properties
- Mean bias and RMSE of climatological ALT between simulations and observations are significantly reduced with updated model version

24 **Abstract**

25 Besides soil hydrology and snow processes, the NASA Catchment Land Surface Model (CLSM)
26 simulates soil temperature in six layers from the surface down to 13m depth. In this study, to
27 examine CLSM's treatment of subsurface thermodynamics, a baseline simulation produced
28 subsurface temperatures for 1980-2014 across Alaska at 9-km resolution. The results were
29 evaluated using in situ observations from permafrost sites across Alaska. The baseline
30 simulation was found to capture the broad features of inter- and intra-annual variations in soil
31 temperature. Additional model experiments revealed that: (i) the representativeness of local
32 meteorological forcing limits the model's ability to accurately reproduce soil temperature, and
33 (ii) vegetation heterogeneity has a profound influence on subsurface thermodynamics via
34 impacts on the snow physics and energy exchange at surface. Specifically, the profile-average
35 RMSE for soil temperature was reduced from 2.96°C to 2.10°C at one site and from 2.38°C to
36 2.25°C at another by using local forcing and land cover, respectively. Moreover, accounting for
37 the influence of soil organic carbon on the soil thermal properties in CLSM leads to further
38 improvements in profile-average soil temperature RMSE, with reductions of 16% to 56% across
39 the different study sites. The mean bias of climatological ALT is reduced by 36% to 89%, and
40 the RMSE is reduced by 11% to 47%. Finally, results reveal that at some sites it may be essential
41 to include a purely organic soil layer to obtain, in conjunction with vegetation and snow effects,
42 a realistic “buffer zone” between the atmospheric forcing and soil thermal processes.

43

44 **1. Introduction**

45 Permafrost dynamics play a vital role in the water, energy and carbon cycles. Climate variability
46 predominately controls the general patterns of permafrost occurrence and evolution at regional to
47 global scales. At the local scale, many factors, including complex topography, soil type,
48 vegetation and snow cover also strongly affect the thermal state of the subsurface. In situ
49 permafrost measurement networks that provide near-surface and borehole temperature
50 observations are critical for monitoring local permafrost conditions at the point scale [e.g.,
51 *Hinkel and Nelson* [2003], *Molders and Romanovsky* [2006], *Osterkamp and Romanovsky*
52 [1999], *Romanovsky and Osterkamp* [1995, 1997], *Romanovsky et al.*[2010], *Shiklomanov et*
53 *al.*[2010]]. However, in situ data are still too sparse in space and in time to allow their extensive
54 use for monitoring permafrost at the regional scale, particularly in areas with a harsh
55 environment and climate, such as Alaska.

56

57 Remote sensing techniques offer an alternative approach to monitoring the extent and
58 distribution of permafrost at the regional scale. Specifically, remote sensing can detect (i) the
59 surface expression of underground permafrost dynamics [*Farquharson et al.*, 2016; *Jones et al.*,
60 2011; *Panda et al.*, 2010], (ii) the freeze/thaw state based on microwave dielectric properties
61 [*Frolking et al.*, 1999; *Kim et al.*, 2011; *Kimball et al.*, 2004; *Kimball et al.*, 2001; *Rautiainen et*
62 *al.*, 2014; *Zhao et al.*, 2011] and (iii) the active layer thickness (ALT) based on measurements of
63 surface subsidence [*Liu et al.*, 2012; *Liu et al.*, 2010]. The obvious drawback of remote sensing
64 techniques, however, is that they cannot directly detect permafrost in the deep subsurface.

65

66 Other approaches for monitoring permafrost and/or the ALT include empirical, equilibrium and
67 numerical modeling methods, as categorized in *Riseborough et al.* [2008]. Empirical methods
68 estimate permafrost response to climate and environmental factors (e.g. soil properties, soil
69 wetness, vegetation, etc.), such as geographically weighted regression methods [*Mishra and*
70 *Riley, 2014*] and spatial analytic techniques based on the Stefan solution [*Nelson et al., 1997;*
71 *Shiklomanov and Nelson, 2002; Zhang et al., 2005*], and usually require site-specific information
72 to develop regression relationships. Equilibrium methods translate air temperature data into
73 estimates of ground temperature and ALT [*Romanovsky and Osterkamp, 1995; Sazonova and*
74 *Romanovsky, 2003*] and are typically suitable only for systems with limited complexity [*Jafarov*
75 *et al., 2012*].

76

77 Numerical modeling, in contrast, is not subject to the above limitations and can be an effective
78 method to describe permafrost dynamics at regional to global scales with the unique advantage
79 of being able to forecast the permafrost response to and feedback on climate change [*Jafarov et*
80 *al., 2012*]. However, numerical modeling requires realistic process parameterizations and
81 accurate data to characterize the local topography, soil characteristics, land surface cover, and
82 micro-climate [*Duguay et al., 2005*]. With recent advances in the development of the necessary
83 databases and improved model physics, numerical models, including Earth system models, have
84 become increasingly useful for estimating permafrost [*Jafarov et al., 2012; Riseborough et al.,*
85 *2008*]. For instance, numerical modeling studies have shown permafrost degradation in Alaska
86 [*Jafarov et al., 2012; Lawrence and Slater, 2005*]. However, more work is needed to quantify the
87 skill of Earth system models to estimate permafrost conditions. Recent efforts to improve
88 permafrost modeling have addressed using a deeper soil column [*Alexeev et al., 2007; Lawrence*

89 *et al.*, 2008], incorporating a surface organic layer [Nicolksy *et al.*, 2007], and accounting for the
90 impact of soil organic carbon on the thermal and hydrologic properties of the soil [Lawrence and
91 Slater, 2008]. In addition, models would benefit from an improved representation of the sub-
92 grid variability of land surface properties such as vegetation properties and soil characteristics
93 [Riseborough *et al.*, 2008].

94

95 In this paper, we systematically assess and improve the ability of a global land surface model
96 (namely, the NASA Catchment Land Surface Model, or CLSM) to represent permafrost
97 conditions in Alaska, extending through a more focused analysis the earlier and more limited
98 evaluation of CLSM's permafrost performance included in Stieglitz *et al.* [2001]. Specifically,
99 this work aims to (i) assess the performance of soil temperature profile estimates (and thus
100 permafrost conditions) simulated by CLSM in Alaska, (ii) investigate the uncertainty associated
101 with the meteorological forcing, land cover, and soil thermal parameter inputs, and (iii) improve
102 the skill of CLSM for simulating permafrost dynamics.

103

104 **2. Theoretical Background and Model Configuration**

105 Permafrost is modeled here using CLSM [Ducharne *et al.*, 2000; Koster *et al.*, 2000], the land
106 model component of the NASA Goddard Earth Observing System (GEOS-5) coupled Earth
107 system model. Here, CLSM is used in an off-line (land-only) configuration. The CLSM
108 subsurface heat transfer module uses six soil layers, each with its own prognostic heat content.
109 For the land cover classes considered in this discussion, these six subsurface layers lie below a
110 negligibly thin surface (skin) layer from which surface radiative and turbulent fluxes are

111 computed. (As described by *Koster et al.* [2000], this surface layer in fact features three
112 horizontally distinct temperatures tied to horizontally-varying hydrological regime.) The soil
113 thickness for each subsurface layer increases with depth; the relevant depths are 0~0.1m,
114 0.1~0.3m, 0.3~0.7m, 0.7~1.4m, 1.4~3m, and 3~13m from top to bottom, respectively. Snow
115 acts as a buffer that modulates the heat and water exchange between the overlying air and the
116 underlying land surface and is simulated using a three-layer snow model that tracks the evolution
117 of snow mass, snow depth, and snow heat content [*Stieglitz et al.*, 2001].

118

119 In the following, we outline the theoretical background of the soil heat transfer module in CLSM
120 (section 2.1) and the current parameterization for soil thermal conductivity (section 2.2).
121 Thereafter, we describe changes to the model parameterization that are designed to improve the
122 simulation of permafrost (section 2.3). Finally, we discuss the model domain and ancillary
123 forcing data (section 2.4).

124

125 **2.1 Heat Transfer**

126 Heat transfer in the subsurface is governed by the one-dimensional heat diffusion equation (Eq.
127 1):

$$C \frac{\partial T(z, t)}{\partial t} = \frac{\partial}{\partial z} \left(\lambda \frac{\partial T(z, t)}{\partial z} \right) \quad (\text{Eq. 1})$$

128 where C is the volumetric heat capacity ($\text{Jm}^{-3}\text{K}^{-1}$), which is equal to the sum of the specific heat
129 capacities of the soil constituents (water, ice, soil minerals, organic matter, and air) multiplied by
130 their respective volumetric fractions. The soil temperature at depth z and time t is denoted as

131 $T(z, t)$ (K), and λ is the soil thermal conductivity ($\text{W m}^{-1} \text{K}^{-1}$), which also varies with depth and
132 time. Using a finite-difference method, the heat diffusion equation (Eq. 1) can be discretized and
133 approximately solved using

$$H(l, t + 1) = H(l, t) + (F(l + 1) - F(l))\Delta t \quad (\text{Eq. 2})$$

134 where $H(l, t)$ represents the heat content associated with soil layer l (J m^{-2}), with a zero
135 reference value corresponding to a layer holding liquid water at exactly 0°C (so that “negative”
136 heat contents imply the presence of ice and, potentially, subfreezing temperatures).

137

138 $H(l, t)$ is related to the temperature $T(l, t)$ and the fraction of ice in the layer, $f_{ice}(l, t)$, through
139 consideration of the heat capacity, C , and the assumed amount of water, W , in the soil that can
140 freeze or melt. The ice fraction is computed first:

$$141 \quad f_{ice}(l, t) = 0. \quad \text{if } H(l, t)/(L_s W) > 0.$$

$$142 \quad f_{ice}(l, t) = 1. \quad \text{if } H(l, t)/(L_s W) < -1. \quad (\text{Eq. 3})$$

$$143 \quad f_{ice}(l, t) = -H(l, t)/(L_s W) \quad \text{otherwise.}$$

144 L_s here represents the latent heat of fusion. With the ice fraction known, we can compute $T(l, t)$,
145 expressed here in degrees Celsius:

$$146 \quad T(l, t) = H(l, t) / C \quad \text{if } f_{ice}(l, t) = 0$$

$$147 \quad T(l, t) = (H(l, t) + L_s W) / C \quad \text{if } f_{ice}(l, t) = 1 \quad (\text{Eq. 4})$$

$$148 \quad T(l, t) = 0 \quad \text{otherwise.}$$

149

150 The heat flux $F(l)$ due to heat diffusion along the temperature gradient between layer $l-1$ and l
151 (Wm^{-2}), for use in (1), is expressed as

$$F(l) = K \frac{\Delta T}{\Delta z} = K \frac{T(l,t) - T(l-1,t)}{zc(l) - zc(l-1)} \quad (\text{Eq. 5})$$

152 where $K = \frac{[zb(l) - zc(l-1)]\lambda(l-1) + [zc(l) - zb(l)]\lambda(l)}{zc(l) - zc(l-1)}$ is the depth-weighted thermal conductivity
153 ($\text{Wm}^{-1}\text{K}^{-1}$) between layers l and $l-1$, $zb(l)$ represents the depth at the top of layer l , and $zc(l)$ is
154 the depth at the center of layer l .

155

156 Eq. 2 is solved using an explicit approach, that is, the soil temperatures at the current time step
157 are determined from the heat contents (the model's prognostic variables) at the previous time
158 step using (Eq. 3) and (Eq. 4) above. The heat flux at the uppermost soil boundary is equal to the
159 ground heat flux, which is obtained by solving the surface energy-balance equation. A no-heat-
160 flux boundary condition is applied at the lowest boundary (i.e., at $\sim 13\text{m}$ depth). The key model
161 parameters impacting the soil heat transfer is the thermal conductivity, which is further described
162 in the next section.

163

164 **2.2 Baseline Soil Thermal Conductivity Parameterizations**

165 The soil thermal conductivity parameterization in CLSM is based on *Johansen* [1977] and
166 *Farouki* [1981]. Specifically, the thermal conductivity λ of unsaturated soil is a weighted average
167 of the saturated and dry thermal conductivities:

$$\lambda = K_e \lambda_{sat} + (1 - K_e) \lambda_{dry} \quad (\text{Eq. 6})$$

168 where K_e is the Kersten number, which is related to the degree of saturation of the soil layer
 169 [Johansen, 1977]. In CLSM, the soil water model component is only loosely coupled with the
 170 soil heat transfer component. The baseline CLSM version uses a constant saturation for the
 171 calculation of the thermal conductivity under unsaturated conditions, assuming that the soil water
 172 is always at 50% of saturation regardless of the modeled soil water conditions; that is, $K_e = 0.5$.
 173 Below the water table, fully saturated conditions are assumed. For the layer that contains the
 174 water table, the Kersten number is computed as $K_e = (\Delta z_1 * 0.5 + \Delta z_2) / (\Delta z_1 + \Delta z_2)$, where Δz_1 and
 175 Δz_2 are the partial layer thicknesses above and below the water table, respectively. In general,
 176 the computation of K_e is inconsistent with the modeled soil moisture conditions.

177

178 The thermal conductivity for dry soil, λ_{dry} , has the form

$$\lambda_{dry} = 0.039 \times n^{-2.2} \quad (\text{Eq. 7})$$

179 where n is the porosity, which is assumed to be 0.45 in the baseline CLSM version for the
 180 calculation of λ_{dry} . Thus, $\lambda_{dry} = 0.226 \text{ W m}^{-1} \text{ K}^{-1}$ regardless of soil type. (Note that CLSM uses
 181 soil texture-dependent porosity values [De Lannoy *et al.*, 2014] for modeling soil moisture
 182 dynamics.) Finally, the thermal conductivity of saturated soil, λ_{sat} , is computed as

$$\lambda_{sat} = \lambda_s^{(1-n)} \lambda_i^{(n-w_u)} \lambda_w^{w_u} \quad (\text{Eq. 8})$$

183 where λ_w , λ_i and λ_s are the thermal conductivities for liquid water ($0.57 \text{ Wm}^{-1}\text{K}^{-1}$), ice ($2.2 \text{ Wm}^{-1}\text{K}^{-1}$), and soil solids ($3 \text{ Wm}^{-1}\text{K}^{-1}$ in CLSM), respectively. The fractional volume of liquid
184 water, w_u , is calculated as $w_u = n * (1 - f_{ice})$, where f_{ice} is the ice fraction.
185

186

187 **2.3 Model Improvements**

188 While the essential physical processes for soil heat transfer are considered in the baseline CLSM
189 (section 2.2), three underlying assumptions potentially impair the model's ability to accurately
190 simulate permafrost dynamics. The first assumption is the use of a constant soil water saturation
191 of 0.5 for the calculation of the thermal conductivity under unsaturated conditions, which
192 neglects the impact of soil water dynamics on the thermal processes. λ_{dry} and λ_s The second is
193 the use of a constant soil water saturation of 0.5 for the calculation of the heat capacity, C. The
194 third is the use of constant thermal conductivity values for λ_{dry} and λ_s regardless of soil mineral
195 type and organic carbon content. Each of these issues was addressed in turn in the development
196 of an improved treatment of subsurface heat transport.

197

198 To address the first issue, we modified CLSM to use the dynamically-varying modeled soil
199 moisture estimates in the calculation of the thermal conductivity (Eq. 6). As a result, the updated
200 CLSM now allows for more efficient heat transport when the soil is wetter. This modification of
201 the code is employed in all of the simulations described in section 5.

202

203 Addressing the second issue with code modifications is not nearly as straightforward. As soon as
204 heat capacity becomes a function of soil moisture content, energy balance calculations become

205 significantly more complex, given that a proper energy balance requires that the energy attached
206 to the dynamic water variable be transported with this water as it diffuses, drains, or is extracted
207 for transpiration, all in addition to or in conjunction with energy transport through heat diffusion.
208 Given the unusual water variables in CLSM – they are not strictly tied to soil layers, as in other
209 LSMs, and in any case they are not coincident with the vertical temperature discretization – such
210 energy-in-water accounting would quickly become intractable. In the face of these issues, we
211 addressed the question of heat capacity instead with a series of five sensitivity experiments,
212 assigning to a given experiment a non-dynamic specific heat capacity associated with one of five
213 different water contents: $w = 0., 0.25, 0.5, 0.75$ and 1, where w is the soil's degree of saturation.
214 The time series over multiple years of simulated subsurface temperatures at a representative site
215 were found to be largely insensitive to the heat capacity employed, particularly for $w \geq 0.25$ (see
216 Figure S1 in the supplementary file). In light of this insensitivity, we retain the original
217 assumption of $w=0.5$ for the calculation of the constant specific heat capacity, recognizing the
218 potential for some error in very dry conditions (which are, in any case, relatively rare in
219 permafrost areas).

220

221 To address the final issue above, we adopt a revised parameterization for the soil thermal
222 properties that incorporates the impact of soil organic carbon based on *Lawrence and Slater*
223 [2008]. In the revised parameterization, soil thermal properties are calculated as:

$$x = (1 - f_{sc})x_{mineral} + f_{sc}x_{sc} \quad (\text{Eq. 9})$$

224 where x represents a soil thermal property such as λ_s , λ_{dry} , the specific heat capacity of soil
225 solid c_s , or the soil porosity that is used in heat transfer module. The corresponding thermal

226 properties for mineral soil and soil carbon are denoted with $x_{mineral}$ and x_{sc} , respectively. The
227 soil carbon fraction f_{sc} is described in more detail in section 3.2. To be consistent with
228 *Lawrence and Slater* [2008], we further set the Kersten number to the degree of saturation
229 ($Ke = S_r$) under frozen conditions and to $Ke = \log(S_r) + 1$ for thawed conditions (though we
230 constrain it to lie between 0 and 1). This implies, however, that the soil porosities used for the
231 soil thermal calculations (Eq. 7) differ from the porosities [*De Lannoy et al.*, 2014] used in the
232 soil water module. The results with this revised CLSM version are discussed in section 5.3.

233

234 **2.4 Model Domain and Ancillary Data**

235 Although CLSM is typically used as a global model, we focus here on Alaska, where continuous,
236 discontinuous, and sporadic permafrost conditions exist in areas ranging from the North Slope to
237 the southern glacial, high-mountain region [*Duguay et al.*, 2005; *Zhang et al.*, 1999]. Alaska is a
238 useful study area because suitable in situ observations are available for validation there (section
239 3.1). Figure 1a shows the model domain used here along with the elevation from the GEOS-5
240 modeling system [*Mahanama et al.*, 2015]. Figure 1b shows the 2-m air temperature
241 climatology, calculated by averaging 35 years of data (1980-2014) from the Modern-Era
242 Retrospective Analysis for Research and Applications-2 [MERRA-2; *Bosilovich et al.*, 2015]
243 reanalysis. From north to south, the annual average air temperature ranges from about -10.8°C to
244 6.4°C. Figure 1c displays a map of permafrost extent in Alaska, showing four types of
245 permafrost: continuous (90-100%), discontinuous (50- 90%), sporadic(10- 50%) and isolated
246 patches (0 - 10%) [*Brown et al.*, 2002].

247

248 We conducted a baseline simulation at 9-km resolution for the entire domain from 1980 to 2014
249 using the baseline version of the CLSM. The model configuration within this system is similar
250 to that used in the Soil Moisture Active Passive Level 4 Soil Moisture algorithm [Reichle *et al.*,
251 2016]. The model was forced with hourly surface meteorological forcing data from MERRA-2
252 [Bosilovich *et al.*, 2015; *Global Modeling and Assimilation Office (GMAO)*, 2015a, 2015b]. The
253 precipitation forcing used here is essentially a rescaled version of the precipitation generated by
254 the atmospheric general circulation model within the MERRA-2 system [Reichle *et al.*, 2017],
255 with the (uncorrected) MERRA-2 precipitation rescaled to the long-term, seasonally varying
256 climatology of the Global Precipitation Climatology Project version 2.2 (GPCP v2.2) product.
257 (At latitudes south of 62.5°N, some information from the 0.5° degree, global Climate Prediction
258 Center Unified gauge product is used as described in Reichle *et al.* [2017], but the impact of the
259 gauge data is minimal for the high-latitude domain considered here.) The model was spun up,
260 reaching a quasi-equilibrium, by looping 100 times through the one-year period from 01/01/2014
261 to 01/01/2015 and then once through the 35-year period from 01/01/1980 to 01/01/2015 period.
262 Table 1 describes the land model parameters and boundary conditions used, including soil
263 texture parameters, soil hydraulic parameters, soil depth, land cover, vegetation height, leaf area
264 index (LAI), greenness fraction, and albedo [Mahanama *et al.*, 2015].

265

266 **3. Datasets**

267 **3.1 In situ Permafrost Observations**

268 To evaluate the simulation results and assess model performance, we used measurements from
269 51 active permafrost sites in Alaska [Romanovsky *et al.*, 2009]

270 (http://permafrost.gi.alaska.edu/sites_map; see dots in Figure 1). Most of the permafrost sites are
271 equipped with sensors that provide daily measurements of the soil temperature profile down to
272 0.5m~3m below the surface. The few sites that only have intermittent, deeper borehole
273 observations down to 50m~60m are not used here. The in situ soil temperature observations
274 were interpolated to the center of each CLSM layer using an Inverse Distance Weighting
275 method. The aggregated daily soil temperature observations were then used for comparison with
276 simulated, layer-based soil temperatures.

277

278 Problematic data records were screened out during a quality control review process. Simple cases
279 include temperature values that were outside of the valid range as well as missing and null
280 records. Moreover, we noticed some systematic errors. For instance, portions of some records
281 exhibited an unnatural phase shift with respect to the corresponding multi-year climatology. It
282 might be possible to use these records after correcting for the unnatural time shift, but in our
283 work we simply excluded the affected measurements from the validation.

284

285 **3.2 Soil Organic Carbon Database**

286 We estimated vertical profiles of soil carbon fraction (f_{sc}) from two datasets that provide soil
287 carbon content. The first dataset is the Global Gridded Surfaces of Selected Soil Characteristics
288 product developed by the Global Soil Data Task Group of the International Geosphere-Biosphere
289 Programme Data and Information System (IGBP-DIS) [Carter and Scholes, 2000; *Global Soil*
290 *Data Task*, 2000; Scholes *et al.*, 1995]. The IGBP-DIS data cover the top 1.5m of the soil at
291 0.083° spatial resolution. The second dataset is the Northern Circumpolar Soil Carbon Database

292 version 2 (NCSCD) [*Hugelius et al.*, 2013a; *Hugelius et al.*, 2014; *Hugelius et al.*, 2013b]. The
293 NCSCD product is at finer resolution (0.012°) and covers the top 3m of soil providing data for
294 the 0-0.3m, 0-1m, 1-2m and 2-3m depth ranges.

295

296 We interpolated the soil carbon content (kg m^{-2}) data to the 9-km model grid using the nearest
297 neighbor method for both IGBP-DIS and NCSCD data. For the NCSCD data, simple aggregation
298 of data for the 0~1m and 1~2m depth range was employed to obtain total carbon content in the
299 top 2m. Next, we calculated the soil carbon density ρ_{sc} (kg m^{-3}). Following *Lawrence and*
300 *Slater* [2008], we adopted the cumulative carbon storage profile for polar and boreal soils as
301 identified in *Zinke et al.* [1986] to estimate vertical distribution (Vd) of soil carbon content. The
302 soil carbon fraction for the l -th layer, $f_{sc}(l)$, was thus computed as $\rho_{sc}(l)/\rho_{sc,max}$, where ρ_{sc} is
303 soil carbon density in the l -th layer calculated as $SCC \times Vd(l)/\Delta z(l)$, SCC is the soil carbon
304 content, and $\rho_{sc,max}$ is the maximum soil carbon density. The latter is set to the standard value
305 for the bulk density of peat, 130kg m^{-3} [*Farouki*, 1981].

306

307 **3.3 Weather Station Data**

308 Weather station data were obtained from the Quality Controlled Local Climatological Data
309 product, which provides hourly-to-monthly records and is available at the National Centers for
310 Environmental Information (NCEI; <http://www.ncdc.noaa.gov/orders/qclcd/>). Specifically, we
311 extracted measurements of dry bulb temperature, wet bulb temperature, dew point, relative
312 humidity, wind speed, air pressure, and precipitation. Moreover, we downloaded and processed
313 solar radiation measurements at weather stations from the National Solar Radiation Database at

314 NCEI (<ftp://ftp.ncdc.noaa.gov/pub/data/nsrdb-solar/solar-only/>). The weather station
315 measurements were used to assess the MERRA-2 surface meteorological forcing data and to
316 improve the forcing data by simple scaling methods (section 5.1).

317

318 Unfortunately, owing to the harsh environmental conditions, it is difficult to maintain weather
319 stations in the high latitudes, particularly at high elevations, and this results in poor spatial and
320 temporal coverage. In addition, due to the complex topography and micro-climates commonly
321 found in Alaska, a particular weather station is often not representative of conditions within an
322 associated 9-km grid cell. This is especially true for the interior of Alaska. Only one station,
323 Deadhorse airport (Site ID: 70063727406), is co-located (within a distance of about 3.5 km) with
324 a permafrost site (DH1) and could thereby be used in this study.

325

326 **4. Assessment of Baseline Results**

327 The baseline simulation was conducted using the original version of CLSM (section 2.2) for the
328 period 1980 to 2014. Figure 2a illustrates the soil freeze/thaw variability in space and time using
329 baseline simulated soil temperature at 8:30pm (local time) on the 16th day of every other month
330 in 2014 as a typical example. The figure shows that for large regions the top three layers are
331 frozen (indicated by the gray color) in late winter (February). The 4th and 5th layers continue to
332 freeze into April whereas the top two layers are already starting to thaw in early spring. During
333 the summer, the near-surface soil continues to thaw, and by August the top three layers are
334 completely thawed while the 4th layer remains frozen in some parts of the North Slope. With the
335 start of the cold season in October, the soil starts to re-freeze from the top down. Note that the

336 4th layer is much warmer compared to the upper layers during winter, and the re-freezing cycle in
337 the 5th layer has an even greater time lag. The lagged freeze/thaw cycle in the different soil
338 layers is also illustrated in Figure 2b, which shows, for each layer, the daily climatology of the
339 frozen area in the domain. The shaded area indicates the inter-annual variability across the 35-
340 year simulation period. The figure shows that the frozen area in the top three layers reaches zero
341 around June. The 4th through 6th layers show much smaller seasonal variability compared with
342 the upper layers, owing to the higher heat capacity in the deeper (thicker) layers. In the
343 remainder of this section, we use the observations at the in situ permafrost sites (section 3.1;
344 Figure 1a) to validate the simulated ALT (section 4.1) and soil temperature profiles (section 4.2).

345

346 **4.1 Evaluation of Simulated Active Layer Thickness**

347 Simulated ALT values were calculated for each year in the 35-year period based on (1) the
348 model-simulated soil temperature profiles and (2) the ice content within the uppermost soil layer
349 that is at least partially frozen. If the entire soil column remains thawed year-round, the
350 simulated ALT is set to null (that is, permafrost-free). The spatial patterns of the 35-year
351 minimum, mean, and maximum annual ALT in Alaska are shown in Figure 3a. Generally, the
352 spatial permafrost distribution is consistent with the permafrost map shown in Figure 1c. Most of
353 the continuous permafrost extent is captured by the model simulation, while some of the
354 discontinuous and sporadic permafrost areas are not, perhaps due to model's coarse resolution.
355 The spatial ALT pattern is also similar to that of previous studies [e.g. *Mishra and Riley, 2014;*
356 *Sazonova and Romanovsky, 2003*] with relatively shallow ALT in the north and deeper values in
357 the interior. Figure 3a also indicates that there is no permafrost in some southern areas of the
358 domain (gray areas). This is consistent with the air temperature climatology (Figure 1b), which

359 indicates annual average temperatures above -2°C. (Note that the effective annually-averaged
360 temperature forcing is in fact slightly higher there given that the insulating properties of snow
361 help shield the subsurface from cold winter air temperatures.) The permafrost-free areas may
362 include patches of sporadic or isolated permafrost [Zhang *et al.*, 1999], but such patches are not
363 resolved in the simulation owing to the relatively coarse (9-km) model resolution. Considering
364 this, the permafrost-free area can be interpreted as indicative of having a low probability of
365 permafrost, which is also consistent with the permafrost probability results reported by *Pastick et*
366 *al.*[2015]. The temporal variations in the spatial mean air temperature and ALT (Figure 3b) are
367 consistent for some years but show a lagged pattern (on the order of one year) for other years,
368 depending on the magnitude of the temperature changes, which is reasonable. The figure
369 suggests a decline in the regionally averaged ALT since 2010, but overall there is a slightly
370 increasing trend in the regional ALT that is consistent with the increasing air temperature trend
371 over the 35 years. The trend line of regional ALT has a positive slope suggesting an increasing
372 rate about 0.4cm per year, and the warming rate for air temperature is about 0.02°C per year as
373 shown in Figure 3b.

374

375 To validate the simulated ALT, multi-year average ALT values were calculated from the in situ
376 soil temperature observations at the permafrost measurements sites. Figure 4 shows a scatter
377 plot between the simulated and observed multi-year mean ALT values, along with the spatial
378 distribution of the ALT values at the permafrost sites. The model clearly overestimates ALT at
379 most sites compared to the observations, by an average of 0.36m. An outlier site IM1 has a
380 deeper ALT in the observations (1.81m) than in the simulation (0.62m). Note that pixels that
381 were permafrost-free in the simulation were excluded from the comparison. Thus, there are only

382 38 sites presented here. That is, among the 51 active permafrost sites, there are 13 sites for which
383 the baseline simulation is permafrost free but observations show permafrost. It should be stressed
384 that the model performances at these 13 sites are in fact the worst and that this is not reflected in
385 the bias calculation. In the following, we carefully evaluate the modeled soil temperature results
386 and then identify the key issues to address in our model simulations.

387

388 **4.2 Evaluation of Simulated Soil Temperature Profiles**

389 Daily estimates of the simulated soil temperature profiles were evaluated using observations
390 from the permafrost sites (section 3.1). In addition to computing RMSE values for each layer, we
391 also calculated a single, vertically-averaged RMSE value for each site with weights given by the
392 layer thicknesses. This profile-average RMSE assigns more weight to the deeper (thicker)
393 layers. The profile-average RMSE includes only layers for which measurements are available,
394 which is rarely the case for the 6th layer. This single statistic for each observation station permits
395 a convenient, comprehensive assessment of the model's ability to capture subsurface heat
396 transfer processes.

397

398 Generally, the baseline simulation results show fair performance at the regional scale (Figure
399 5a) with a spatially averaged RMSE of 3.48 °C (indicated by the horizontal red line in the
400 figure). The performance varies from site to site with a minimum RMSE of 0.83 °C at COW and
401 a maximum RMSE of 6.52 °C at S3-AWS. Sites within the same 9-km model grid cell
402 (indicated by the background shading in Figure 5a) can exhibit large differences in performance.
403 For instance, sites SL1, SL2, SL3, SL4 and UF1 are within a same model grid cell but have

404 RMSE values ranging from 2.29°C at SL3 to 4.49°C at SL4, demonstrating the large
405 heterogeneity in local site conditions that cannot be captured by the model as applied here.
406 Similarly, sites COF, COS, COT and COW have quite different RMSE values of 3.39°C, 4.00°C,
407 0.96°C and 0.83°C, respectively. The smallest RMSE at COW is attributed to the better
408 simulation in the 2nd and 3rd layers compared to the other sites (Figure 5b). Note that most sites
409 do not have RMSE values for the 5th and 6th layers due to lack of measurements.

410

411 The RMSE values of the 51 sites are mapped in Figure 5c. The figure suggests that, overall, the
412 baseline simulation results show relatively better performance (blue and green colors) along or
413 near the coastline and relatively worse performance in the interior of Alaska (yellow and red
414 colors). This is possibly because the coastal areas generally have a less variable climate and, in
415 the northern part of Alaska, less complex terrain than the interior. Coastal areas are thus better
416 represented by the meteorological forcing data and the land model parameters from the GEOS-5
417 system. The greater heterogeneity in micro-climate, orographic effects, and landscape vegetation
418 gradients in the interior region is less well described by the global-scale input data.

419

420 We selected 9 sites (as labeled in Figure 5c) for further investigation of these aspects, including a
421 site that is close to the northern coast (DH1), three sites along the northern highway (FB1, SG2
422 and GL1), and five sites in the interior near Fairbanks (UF1, SL1, SL2, SL3 and SL4). The latter
423 are located within the same 9-km model grid cell. The sites were selected primarily because of
424 the availability of (1) soil temperature measurements in each soil layer, (2) long measurement

425 records, and (3) local soil information. Geolocation and land surface information for the selected
426 sites are provided in Table 2.

427

428 Our ultimate objective for investigating these 9 sites more closely is to improve the model's skill
429 in reproducing the subsurface soil temperature profile. Specifically, DH1 is used to investigate
430 the impact of errors in the MERRA-2 meteorological forcing data because there is a suitable
431 weather station nearby (section 3.3). UF1 is used to study the influence of land cover type on
432 permafrost simulation because its land cover is distinct from that of the other sites within the
433 same 9-km model grid cell. For the remainder of the sites, including FB1, SG2, GL1, SL1, SL2,
434 SL3 and SL4, soil survey information is available, permitting us to examine the impact on the
435 model skill of using soil carbon information in the calculation of the soil thermal properties.

436

437 **5. Towards Improving Permafrost Modeling**

438 As mentioned in section 2.2, all of the experiments below, with the exception of the baseline
439 experiment, use an updated model version that allows the simulated soil moisture dynamics to
440 affect the thermal conductivity calculation (specifically, the Kersten number). Results obtained
441 during the development of this version demonstrate that this facet of the model physics has only
442 a marginal impact on modeled soil temperatures (not shown). We now evaluate the impact of
443 three more important facets of the permafrost modeling problem: (1) the accuracy of the
444 meteorological forcing (section 5.1), (2) the choice of land cover (section 5.2), and (3) the
445 assigned soil thermal properties (sections 5.3 and 5.4).

446

447 In examining these three aspects, we essentially break down the heat transfer process into two
448 vertical gradients [Koven *et al.*, 2013]. The first gradient (the “air to shallow soil” gradient)
449 determines the heat transfer from the atmosphere to the shallow soil and is controlled in part by
450 the meteorological forcing and land cover type. The second gradient (the “shallow to deep soil”)
451 gradient) is associated with heat transfer from shallow to deep soils and is controlled by the soil’s
452 thermal properties.

453

454 **5.1 Meteorological Forcing**

455 The evaluation of simulated 9-km grid cell-scale subsurface temperatures with point-scale in situ
456 measurements is subject to scaling uncertainty. This is exacerbated by the coarse resolution of
457 both the MERRA-2 meteorological forcing and the applied land surface parameters. Consider,
458 for example, the five sites UF1 and SL1-4, as marked in Figure 5b. Although the UF1 and SL
459 sites are within the same model grid cell (9-km) and thus use the same meteorological forcing in
460 our simulations, the observed soil temperatures at these sites are markedly different – a result of
461 some unresolved heterogeneity.

462

463 To assess the scaling problem, at least the part associated with meteorological forcing, we
464 obtained local weather data from a weather station co-located with a permafrost site (site DH1;
465 see section 3.3). We then filled the large temporal gaps in the station data using scaled MERRA-
466 2 forcing fields – the original MERRA-2 variables at the grid cell containing the site were scaled
467 with either multiplicative corrections (for specific humidity, wind speed, precipitation and solar
468 radiation) or additive corrections (for air temperature and pressure) so that the climatological

469 monthly means of the MERRA-2 data matched those of the station observations. We then forced
470 the land model with the raw weather station data whenever they were available and with the
471 scaled MERRA-2 data otherwise.

472

473 The multi-year mean seasonal cycles of the simulated subsurface soil temperatures obtained with
474 the original MERRA-2 forcing and with the station-based forcing at DH1 are shown in Figure 6,
475 along with observations. The figure shows that at this site, the original MERRA-2 forcing
476 produces a reasonable simulation of subsurface temperature, capturing much of the observed
477 seasonal cycle. The simulation results improve even further, though, when the station-based
478 forcing fields are fed into the model (black line; see in particular the simulated-minus-observed
479 differences shown in Figure 6b). With the original MERRA-2 forcing, the maximum errors
480 appear in May to July due to a slightly earlier thawing time compared to observations. This
481 problem is effectively alleviated in the simulation using the station-based forcing fields (black
482 vs. gray in Figure 6b). The profile-average RMSE is 2.96°C for the daily soil temperature
483 simulated using the original MERRA-2 forcing, and it reduces to 2.10°C when using the station-
484 based forcing. As for the multi-year mean seasonal cycle, the profile-average RMSE is reduced
485 by 60% (2.53°C vs. 0.95°C). This confirms that the forcing has a first order impact on the
486 simulation of the subsurface temperatures. However, both simulations cannot pick up the zero
487 curtains at the freeze up time around Nov. for the top three layers, which might be associated
488 with some thermodynamic processes currently lacking in the model, such as the advection of
489 heat upward or downward with the diffusion of moisture.

490

491 **5.2 Land Cover**

492 The land cover type chosen for a simulation can affect the energy (and water) partitioning at the
493 land-atmosphere interface and can potentially have a strong impact on the transfer of heat
494 between the air and the shallow soil. To examine this, we consider now the UF1 site near the
495 University of Alaska, Fairbanks. When the land model is run globally (or across Alaska, as in
496 Figure 2), the assigned vegetation class for this particular grid cell (and thus for our baseline UF1
497 simulation) is broadleaf deciduous tree. Site pictures and the site survey, however, indicate that
498 the local land cover at UF1 is more like grassland (<http://permafrost.gi.alaska.edu/site/uf1>).
499 Thus, we performed a new experiment at UF1 with grassland assigned as the surface type and
500 with the associated vegetation height set to 0.6m (as standardly used in this model for grassland
501 conditions). Aside from the aforementioned additional use of a moisture-dependent thermal
502 conductivity, the experiment was otherwise identical to the baseline experiment.

503

504 The results from the two experiments are illustrated in Figure 7. The figure shows that
505 modifying the land cover improves the simulation results at this site; the profile-average RMSE
506 is reduced from 2.38°C for the simulation (“Tree”) to 2.25°C for the new experiment (“Grass”).
507 The improvements are mainly seen in the 5th layer, which indirectly benefits from the better
508 agreement between simulated snow depth for Grass and observations (see the top panel of Figure
509 7). The thicker snowpack generated in the “Grass” experiment acts as a stronger “thermal
510 blanket” that slows down the release of energy from the ground during the cold season, which
511 facilitates warmer, more accurate soil temperatures in the 5th soil layer. For example, the Grass
512 simulation results show very good agreement with observations in the 5th layer in October of
513 2012, while the corresponding temperatures in the Tree experiment are about 3°C colder. In May

514 of 2013, the 5th layer temperatures simulated in the two experiments differ by up to 2.7°C, with
515 solidly frozen soil in the Tree experiment and thawed soil (at 0.01°C) in the Grass experiment.
516 Note that although the simulation of snow depth is more accurate in the Grass experiment, it is
517 still underestimated in that experiment, and thus even this experiment shows earlier thawing
518 compared to the observations. We expect, however, that further improvements could have been
519 achieved by using local meteorological forcing fields (currently unavailable) in the simulations;
520 as discussed in Section 5.1, simulations at DH1 demonstrated better thawing time with station-
521 based forcing.

522

523 The change in the snowpack and the resulting changes in the subsurface temperatures in Figure 7
524 can be explained by the effect of vegetation height on the albedo of snow-covered areas. Because
525 grassland is shorter than forest, less of its structure appears above the snow cover, resulting in a
526 larger albedo for the snowpack; for forests in particular, modeled albedo in the presence of snow
527 is significantly reduced by exposed tree branches and stems. Relative to forests, higher albedos
528 over grassland for a given amount of snow lead to less melting and thus greater snow
529 accumulation.

530

531 Overall, the results for UF1 illustrate the difficulty of using local, in situ measurements to
532 evaluate model simulation results given that the large-scale parameter values assumed for the
533 grid cell (here, values associated with forest cover) may be inconsistent with the local conditions
534 at the measurement site. Although changing the assumed land cover to grassland led to
535 significant improvements at UF1, subsurface temperatures there are still overestimated during

536 summer and underestimated during winter, resulting in still-large inaccuracies in the simulated
537 seasonal cycle. This may very well be due to inaccuracies in the MERRA-2-derived
538 meteorological forcing. The weather station closest to this permafrost site is at the Fairbanks
539 International Airport, about 5.5km away; the approach used above for DH1 to examine the
540 impacts of meteorological forcing is thus not applicable here. Nevertheless, we will address in
541 section 5.3 below how well the model works at UF1 under the assumption of a “perfect” air-to-
542 shallow soil gradient (which would include an assumption of perfect meteorological forcing).

543

544 We now turn our attention to the other sites across Alaska. Inspection of site pictures suggests
545 that most permafrost sites are found within grassy areas even when surrounding conditions are
546 much different. For instance, the SL sites, which are installed in the forested area of Smith Lake
547 near the University of Alaska, Fairbanks, are seen sitting amongst grassland patches within the
548 forest (<http://permafrost.gi.alaska.edu/site/sl4>). This is reasonable given the logistics of
549 installation and maintenance. Again, at UF1, assigning grassland rather than forest characteristics
550 led to an improved simulation of subsurface temperatures; to see if this improvement is seen at
551 other sites across Alaska as well, we repeated the experiment at these other sites. Figure 8a
552 shows the profile-average RMSE from this new experiment (“Grass”) minus that from the
553 baseline simulation (“Baseline”) at all of the sites. In the plot, negative values (blue colors)
554 indicate improvement in model performance through the use of grassland parameters whereas
555 positive values (orange and red colors) indicate degraded performance. While there is a mix of
556 positive and negative differences, the spatial mean of the RMSE difference is negative (- 0.15⁰C)
557 indicating an overall improvement.

558

559 When considering the question of land cover impacts across the various in situ sites across
560 Alaska, we should note that a comprehensive analysis of albedo effects on snow depth and of
561 snow insulation effects on the simulation of permafrost is unfortunately limited by a lack of data,
562 particularly snow depth and total albedo at the sites. (The availability of snow depth data at UF1
563 is one of the few exceptions.) Various ancillary products (e.g., albedo estimates from MODIS)
564 may perhaps contribute information to a comprehensive study.

565

566 We now examine the consistency between improvements in simulating the aforementioned air-
567 to-shallow soil temperature gradient and the shallow-to-deep soil temperature gradient. First, the
568 temperature offset between the top soil layer and the overlying air, Ta_0 , was calculated at the
569 monthly scale; this offset is taken to represent the temperature gradient from the air to the
570 shallow soil. Similarly, the offset, T_01 , between the monthly temperatures in the 4th layer (about
571 1 meter deep) and the top layer was computed to represent the shallow-to-deep soil gradient. We
572 then computed the RMSE of the simulated Ta_0 and T_01 values against site observations for both
573 the baseline and grassland experiments. Figure 8b shows the spatial distribution of the
574 differences between the grassland and baseline experiments in the RMSE for Ta_0 , and Figure 8c
575 shows the corresponding differences for the RMSE of T_01 . As before, negative values indicate
576 improvements associated with the use of grassland parameters.

577

578 Theory suggests that improvements in Ta_0 should translate to improvements in T_01 – deep soil
579 temperature variations are ultimately driven by variations in air temperature, and the deep soil
580 cannot be simulated properly if the forcing from above is inaccurate. Similarly, degraded model
581 performance along the air-to-shallow soil temperature gradient would presumably result in a

582 degraded shallow-to-deep soil temperature gradient. This consistency is generally seen (for all
583 but two sites) in Figure 8b and 8c – locations where Ta_0 improves with the use of grassland
584 conditions also show improvement in T_01 . The agreement supports the idea that the correct land
585 cover type, which directly affects the shallow soil temperature, also eventually leads to improved
586 heat transfer in the deeper soil.

587

588 **5.3 Isolating Subsurface Heat Transport Processes**

589 If the meteorological forcing and land surface parameterizations (including land cover) were
590 perfect in our simulations, the simulation of subsurface temperatures might still be inaccurate
591 due to a deficient parameterization of subsurface heat transport. To isolate these problems, we
592 perform a series of experiments in which the top layer soil temperature is continually forced to
593 agree with top layer soil temperature observations at a site (i.e., the simulated temperatures in the
594 top layer are continually replaced with corresponding measured values). In the model, the top
595 layer temperature is the sole boundary condition driving the evolution of the temperatures in the
596 layers below. By prescribing the time variation of top layer temperature to observations, we
597 effectively sidestep errors in meteorological forcing and surface parameters at a given site,
598 allowing us to focus specifically on how well heat is transported in the subsurface.

599

600 The experiments in which the top layer temperature is prescribed are denoted “T1BC”, meaning
601 that the top soil layer is effectively the upper boundary condition of the model. For these
602 experiments, initial soil temperatures in the other soil layers were also prescribed to
603 observations. The experiment was carried out at sites that have continuous long-period data

604 records in at least the top four layers for at least three consecutive years: UF1, WD1, HV1, FB1,
605 GL1, SG2, and SL1 through SL4. Due to similarity, results for some sites are not shown here;
606 they can be found in the supplementary material.

607

608 The 5th and 6th layers required special treatment for the initialization because most sites do not
609 provide corresponding measurements that deep. If the needed measurements were absent, these
610 layers were initialized to values obtained from a fully spun-up T1BC simulation at that site.
611 Note that this implies a potential source of error; spinning up the T1BC experiments over only a
612 few recent years implies that the often warmer recent forcing temperatures (Figure 3b) are
613 imprinted, perhaps unrealistically, on the 5th and 6th layers. This should be kept in mind when
614 interpreting the T1BC results.

615

616 With a prescribed top layer temperature, the soil temperatures simulated in the layers below
617 should be accurate if the heat transfer mechanism in the subsurface is adequately represented in
618 the model. This is seen to be the case at UF1 as shown in the left panel of Figure 9. Other sites
619 that show very good performance for the T1BC experiments include WD1 and HV1 (see Figures
620 S2 and S3 in the supplementary file). Figure 9 indicates that the treatment of subsurface heat
621 transport is not responsible for the errors in the UF1 simulation shown in Figure 7; these errors
622 must be due to the meteorological forcing or to the treatment of the processes (including
623 parameter values) that control the surface temperature itself. The model apparently represents
624 well the physics of, for example, thermal conductivity and water/ice phase change in the
625 subsurface at these sites (UF1, WD1 and HV1).

626

627 Other sites (FB1, GL1, SG2, and SL1-SL4), however, did not show the same success. As shown
628 in right panel of Figure 9 for SL1 (and in supplementary Figures S4-S9 for the other sites), the
629 T1BC results at these sites overestimate temperature in the warm period (June to September).
630 Moreover, for all sites except for SL1, the summer overestimation eventually leads to an
631 overestimation of temperature in the cold season (winter to early spring; see supplementary file).
632 The SL1 site is in fact unusual in that its cold season subsurface temperatures in the T1BC
633 experiment are greatly underestimated (Figure 9, right panel). For SL1, the problem is rectified
634 in an additional experiment (T2BC) in which the temperatures of both the 1st and 2nd layer are
635 prescribed to observations. With the 2nd layer forced to be accurate as well, the simulated
636 temperatures in the 3rd through 5th layers become realistic (black line in right panel of Figure 9;
637 no observations are available for the 6th layer.). From these results we conclude that for SL1, the
638 treatment of subsurface heat transport in the model is adequate at and below the 3rd layer, but that
639 some aspect of the problem is poorly captured in the top and 2nd layers. The sites FB1, GL1,
640 SG2, SL2, SL3, and SL4 also appear to be deficient specifically in the top two layers, as these
641 sites also show substantial improvement when the 1st and 2nd layers are prescribed to
642 observations (see supplementary Figures S10-S15).

643

644 In summary, subsurface heat transfer appears accurate at a few sites but is deficient at several
645 others, especially in the top and 2nd layer. We address a possible reason in the next section.

646

647 **5.4 Impacts of Organic Carbon**

648 We hypothesize that the errors in the T1BC experiments seen in the right panel of Figure 9 for
649 SL1 and in the supplementary material for several other sites relate to the treatment of organic
650 carbon in the near-surface soil and its impacts on soil thermal conductivity. A rich, organic
651 carbon content is associated with a small soil thermal conductivity, which would impede the
652 insertion of energy into the soil during the warm season and the release of subsurface warmth to
653 the atmosphere during the cold season. Site soil surveys indicate that all of the sites investigated
654 in section 5.3 are organically rich, especially near the surface (Table 2). For instance, peat soil at
655 FB1, SG2 and GL1 exists down to 15cm, 15cm and 55cm, respectively. Although there is no
656 corresponding information available for SL2, SL3 and SL4, the soil survey indicates that at SL1,
657 which is very close to SL2-SL4, peat soil is found down to a depth of 31cm.

658

659 Peat soil is poorly represented in the default model framework. Given the model assumptions
660 regarding soil texture and organic carbon content, the peat soil information in the soil survey
661 suggests that the thermal conductivities used in the default model are excessive, particularly near
662 the surface. The improvement seen for SL1 in the T2BC experiment may even suggest the
663 presence of a purely organic litter layer (e.g., decayed and undecayed leaves) at the site from
664 which the observed top layer temperatures were measured.

665

666 As described in section 3.2, soil carbon fraction profiles were constructed from the IGBP-DIS
667 and NCSCD soil data. Figure 10a illustrates the vertical profiles of soil carbon fraction at the
668 seven sites examined here, including FB1, GL1, SG2, and SL1 through SL4. The profiles

669 derived from the two different carbon datasets are nearly identical at the SL sites but differ
670 significantly at the other sites, especially at SG2. Figure 10b shows the associated soil thermal
671 properties at GL1. The impact of organic carbon content on the soil thermal properties (e.g., the
672 thermal conductivities for soil solids λ_s and dry soil λ_{dry} , the specific heat capacity of the soil
673 c_s , and the soil porosity) are illustrated by the differences between the original CLSM parameters
674 and the new parameters derived from the soil organic carbon databases. With the new soil
675 parameterization, λ_s and λ_{dry} are much smaller in the top two layers. Conversely, c_s and the
676 porosity are much larger than the original CLSM values in the top two layers. In addition, for the
677 new parameters the entire profile of λ_{dry} is much smaller than that of the original CLSM,
678 whereas the porosity is much larger across all layers.

679

680 We incorporated the two different soil carbon fraction profiles into the CLSM using the soil
681 parameterization scheme described in section 2.3. We then re-ran the T1BC experiment at FB1,
682 GL1, SG2, and SL1-4. Results for GL1 and SL2 are shown in Figure 11. The subsurface
683 temperatures obtained in the experiments using the organic carbon profiles (T1BC_OrgC_IGBP
684 and T1BC_OrgC_NCSCD) show an improved agreement with observations during warm periods
685 (June through September) relative to the original T1BC experiment, especially for SL2. Results
686 for sites FB1, SG2, SL3 and SL4 are similar; see supplementary Figures S16-S19. At GL1, for
687 which the two sources of organic carbon profiles differ (see Figure 110), use of the NCSCD
688 information produces the more realistic subsurface temperatures, especially for the 3rd layer.
689 This can be attributed to the larger carbon fraction in the 2nd and 3rd layers at GL1 for NCSCD,
690 as highlighted in Figure 10.

691

692 Figure 12 summarizes the results obtained with the organic content profiles. Compared to the
693 original T1BC results, the profile-average RMSE is reduced for T1BC_OrgC_IBGP and
694 T1BC_OrgC_NCSCD at all six of the study sites, with the better results often obtained with the
695 NCSCD organic content data. The largest improvement in the profile-average RMSE is found at
696 GL1 (about 56%) using NCSCD data. At individual soil layers, improvements are as high as
697 70% (Layer 3 at SL2, again using NCSCD data).

698

699 The behavior at site SL1 is anomalous and merits further discussion. As shown in Figure 12g,
700 both T1BC_OrgC_IBGP and T1BC_OrgC_NCSCD yielded larger profile-average RMSE values
701 than T1BC (i.e., model results were degraded in an aggregate sense) despite considerable
702 improvements during the warm period (see supplementary Figure S20) and a reduction of RMSE
703 for the 2nd and 3rd layers. Nevertheless, both the T1BC_OrgC_IBGP and T1BC_OrgC_NCSCD
704 simulations still cannot capture the large contrast between the soil temperatures in the top and 2nd
705 layers. Furthermore, neither T1BC_OrgC_IBGP nor T1BC_OrgC_NCSCD correct the
706 aforementioned underestimation problem at SL1 during the cold season. Moreover, when the
707 T2BC experiment is performed (i.e., when both the top and 2nd layer temperatures are prescribed
708 to observations), the use of either the IGBP-DIS or NCSCD data still increases slightly the
709 profile-average RMSE relative to the original T2BC experiment (Figure 12h). We can only
710 speculate about this behavior. It is possible, for example, that relative to the cumulative carbon
711 storage profile used to approximate the vertical distribution of carbon content at all sites, the soil
712 carbon content at SL1 is more concentrated in the top two soil layers and much less so in the 3rd
713 and 4th layers. Alternatively, the top two layers might be purely organic layers (a.k.a. litter

714 layers) rather than the assumed composite of mineral soil and organic carbon; this particular
715 explanation is consistent with our analysis in section 5.3.

716

717 Comparison of RMSEs for annual ALT from the different experiments reveals that simulated
718 ALTs improve at six out of the seven test sites when soil carbon impacts are included, as shown
719 in Figure 13 (green vs. cyan and magenta bars for simulations with MERRA-2 forcing, and blue
720 vs. gray and black bars for simulations with prescribed top soil temperature). That is, by
721 incorporating the thermal impacts of soil carbon into the model, simulated ALT is generally
722 improved regardless of the quality of the forcing fields. In addition, despite the larger profile-
723 average RMSE of soil temperature from T1BC compared to the two T1BC simulations
724 incorporating organic carbon at SL1 as discussed above, the annual ALT at this site from
725 baseline and T1BC simulations are significantly improved after incorporating soil carbon
726 impacts. The only exception is SL3, which shows larger RMSE of annual ALT from
727 T1BC_OrgC_IGBP and T1BC_OrgC_NCSCD compared to T1BC. Nevertheless, all seven sites
728 the simulations with MERRA-2 forcing (which is available everywhere and thus suitable for
729 global simulations) demonstrate improved ALT by incorporating soil carbon impacts (cyan and
730 magenta vs. green bars). One thing we should stress again is that for these sites a permafrost-free
731 simulation is an error that cannot be quantified in terms of an RMSE of ALT; any simulation at
732 these sites that has a meaningful ALT (e.g. M2_OrgC_IGBP and M2_OrgC_NCSCD at SLx
733 sites) is a fundamental, if non-quantifiable, improvement over a permafrost-free simulation (e.g.
734 Baseline simulation at SLx sites).

735

736 Figure 13, by the way, also shows that with the original carbon profile, the T1BC simulation
737 tends to produce, as expected, more accurate ALT than the baseline simulation (dark blue versus
738 green bars). We can only speculate on why the MERRA-2 versus T1BC ALT results are
739 relatively mixed for the improved carbon cases (e.g., magenta versus black bars); perhaps it has
740 to do with the aforementioned limitation regarding the spin-up of the 5th and 6th layers in the
741 T1BC experiment.

742

743 Overall, the anomalous results at SL1 and SL3 aside, Figure 11, Figure 12 and 13 support our
744 hypothesis regarding the importance of properly treating the impacts of organic carbon content
745 on soil thermal properties and thereby on subsurface heat transfer – our simulations generally
746 improve with a more careful treatment of organic carbon. The results indicate that the vertical
747 profile of fractional organic matter within the soil composite should be specified realistically, as
748 should the existence of any layers of organic matter sitting on top of the soil layers. A more
749 realistic thermal “buffer zone” should indeed consider both snow and organic layers at some
750 sites.

751

752 We now compare multi-year means of estimated ALT from the three simulations with MERRA-
753 2 forcing (i.e., Baseline, M2_OrgC_IGBP and M2_OrgC_NCSCD) with the observed ALT at all
754 sites across Alaska. The results are shown in Figure 14. Figure 14b shows that the RMSE of
755 multi-year averaged ALT is reduced by 11% and 47% for the simulations using IGBP (0.49m vs.
756 0.55m) and NCSCD (0.29m vs. 0.55m) carbon data, respectively, compared to the baseline
757 simulation. The overall bias values provided in Figure 14c reveal that the M2_OrgC_IGBP
758 simulation still overestimates regional ALT but nevertheless shows a 36% improvement (0.23m

759 vs. 0.36m) over the baseline, while the M2_OrgC_NCS_CD simulation shows a very small
760 negative bias (-0.04m, reduced by 89% compared to 0.36m in terms of absolute bias) in regional
761 ALT, indicating a significant improvement.

762

763 **6. Summary and Discussion**

764 In this study we used the NASA Catchment land surface model to study permafrost conditions in
765 Alaska. We first conducted a regional simulation using the current (baseline) model version and
766 investigated the general pattern and evolution of the simulated permafrost dynamics across
767 Alaska. The modeled ALT shows a large spatial and temporal variability that is consistent with
768 the regional air temperature climatology (Figures 2, 3). However, the modeled ALT is
769 overestimated by ~0.43m on average when compared against in situ observations from 38
770 permafrost measurement sites (Figure 4). The simulated soil temperature profiles have a
771 spatially-averaged, profile-average RMSE of 3.48°C versus the in situ measurements (Figure 5).

772

773 Next, we investigated the soil temperature simulation errors along two vertical temperature
774 gradients, the “air-to-shallow soil” gradient and the “shallow-to-deep soil” gradient. An accurate
775 simulation of the first gradient is a prerequisite for the successful simulation of the subsurface
776 temperature profile. Following this paradigm, we addressed two factors that affect the air-to-
777 shallow soil gradient: (i) the quality of the forcing data and (ii) the land cover representation.
778 Finally, we examined the performance of simulated subsurface heat transfer in isolation (i.e., we
779 focused on the shallow-to-deep soil gradient) by prescribing the temperature in the surface soil
780 layer.

781

782 In the context of our experiments, errors in the model forcing data have two potential sources: (i)
783 inaccuracies in the GEOS-5 atmospheric modeling and assimilation system used to generate the
784 forcing, and (ii) representativeness error, given the relatively coarse (0.5 degree) resolution of the
785 GEOS-5 system and the point scale of the permafrost measurement sites. We addressed both
786 error sources simultaneously by forcing the model at the DH1 site with measurements from a
787 nearby meteorological station. The profile-average RMSE of simulated subsurface temperature
788 at the DH1 site was thereby decreased from 2.96°C to 2.10°C, indicating that, as might be
789 expected, meteorological forcing fields that better reflect the local conditions at a local site
790 produce simulated soil temperature profiles that better agree with observations there.

791

792 Likewise, the model's land cover parameterization may be inaccurate, or the site-specific land
793 cover conditions may not be representative of the grid-cell scale average conditions. In situ
794 measurement sites are usually in more accessible, grassy areas (where snow can build up more
795 easily), whereas larger-scale land cover in the areas studied is more typically forest or shrubs.
796 Our results demonstrate that using grassland parameters rather than the default, grid-average land
797 cover parameters produces soil temperature profiles that better agree with the observations. At
798 the UF1 site, the profile-average RMSE in this experiment decreased from 2.38°C to 2.25°C.

799

800 Finally, we demonstrated that the baseline version of the CLSM can sometimes simulate
801 subsurface thermal dynamics with high accuracy if the top layer temperature is simulated
802 correctly – model simulations that prescribed the surface soil temperature (T1BC) showed

803 success in simulating temperature in the subsurface at a number of sites (UF1, WD1 and HV1).
804 However, at other sites, the T1BC results overestimated the soil temperature, especially during
805 warm periods. For these other sites, the temperatures in both the top and 2nd layers needed to be
806 prescribed to observations (the T2BC experiments) to produce accurate temperatures in the
807 layers below. Overall, the T1BC and T2BC experiments suggest that, while CLSM's treatment
808 of subsurface heat transport below the 2nd layer is accurate, at several sites the soil heat transfer
809 properties in the top two layers of the baseline model are deficient.

810

811 This result led to an examination of the impacts of organic matter, which to date had not been
812 properly considered in the CLSM representation of soil thermal processes. We conducted
813 additional simulations that explicitly included the impact of soil carbon on soil thermal processes
814 using the soil carbon parameterizations of *Lawrence and Slater* [2008]. These simulations
815 utilized carbon data from two data sources (IGBP-DIS and NCSCD) and were run in the T1BC
816 configuration, i.e., with top layer temperatures prescribed to observations. The results show that
817 the more careful treatment of soil organic carbon led to greatly improved simulation results at
818 sites with organic-rich soils. The profile-average RMSE for T1BC_OrgC_NCSCD was reduced
819 by as much as 56% (at GL1) when compared to the original T1BC experiment, and indeed, an
820 RMSE reduction was seen at all of the sites considered in this experiment except for SL1. At
821 SL1, we speculate that the explicit modeling of a strictly organic layer (e.g., composed of leaf
822 litter) may be needed to provide a more effective buffer zone between the air temperature and the
823 deeper soil.

824

825 Simulations with the updated model version driven by MERRA-2 forcing also demonstrated
826 improvements in ALT at the site scale, showing reduced RMSE of annual ALT compared to
827 baseline results. At the regional scale (considering all sites across Alaska), our simulations show
828 reduced RMSE of multi-year averaged ALT compared to the baseline results (by 47%) when
829 NCSCD carbon information is used, along with a very small regional bias (-0.04m). Note that
830 while our RMSE of ALT using NCSCD carbon information (0.29m) is somewhat higher than
831 that found in a similar study by [Jafarov *et al.*, 2012] (0.08m), our model results (unlike theirs)
832 did not benefit from calibration; also, our mean ALT bias (-0.04m) is very close to their value of
833 -0.03m.

834

835 Overall, enhanced treatments of meteorological forcing, land cover type, and organic carbon-
836 related soil thermal properties substantially improved CLSM's ability to simulate realistic
837 subsurface temperatures. Progress toward an effective, large-scale representation of subsurface
838 thermodynamics, however, was nevertheless hampered here by the local-scale character of the in
839 situ measurements and, in any case, by the limited number of measurement sites. Looking
840 ahead, it should be possible to continue model development on a regional, rather than local, scale
841 using radar retrievals of ALT from the Airborne Microwave Observatory of Subcanopy and
842 Subsurface (AirMOSS) instrument [Chen *et al.*, 2016].

843

844 Another issue that has not been addressed fully here but is worth investigating further is the
845 impact of a purely organic layer on subsurface permafrost. Such an organic layer not only has
846 unique thermal properties but also affects soil hydrologic processes by slowing down bare soil
847 evaporation from the ground surface, reducing vegetation transpiration [Luthin and Guymon,

848 1974], altering downslope runoff pathways, and thus significantly affecting soil moisture
849 underneath [Hinzman *et al.*, 1991], which can result in a dramatically different permafrost
850 response. Some key parameters associated with an organic layer can possibly be characterized at
851 the regional scale based on radar remote sensing, such as forthcoming organic layer thickness
852 retrievals from the AirMOSS project (personal communication with Mahta Moghaddam
853 and Richard Chen). Once available, such radar retrievals should make it possible for us to
854 improve further the simulation of permafrost at the regional scale.

855

856 **Acknowledgments**

857 Funding for this work was provided by the NASA Interdisciplinary Science program. We are
858 grateful for valuable discussions with Richard Chen, John Kimball, Mahta Moghaddam, and
859 Yonghong Yi. We thank the two anonymous reviewers for their helpful comments. We
860 acknowledge the University of Maryland supercomputing resources
861 (<http://www.it.umd.edu/hpcc>) made available for conducting the research reported in this paper.
862 Soil temperature observations used in this study are available from the Permafrost Laboratory at
863 University of Alaska Fairbanks (http://permafrost.gi.alaska.edu/sites_map). The IGBP-DIS soil
864 carbon data are available from the Oak Ridge National Laboratory Distributed Active Archive
865 Center (ORNL DAAC) (<https://doi.org/10.3334/ORNLDaac/569>), and the NCSCD dataset is
866 available from the Bolin Centre for Climate Research (<http://bolin.su.se/data/ncscd/>). The
867 weather station data are available at the National Centers for Environmental Information (NCEI;
868 <http://www.ncdc.noaa.gov/orders/qclcd/>). The baseline and revised simulation results are
869 available at <http://hdl.handle.net/1903/20168>.

870 **References**

871 Alexeev, V. A., D. J. Nicolsky, V. E. Romanovsky, and D. M. Lawrence (2007), An evaluation
872 of deep soil configurations in the CLM3 for improved representation of permafrost, *Geophys*
873 *Res Lett*, 34(9), doi:10.1029/2007gl029536.

874 Baret, F., M. Weiss, R. Lacaze, F. Camacho, H. Makhmara, P. Pacholczyk, and B. Smets (2013),
875 GEOV1: LAI and FAPAR essential climate variables and FCOVER global time series
876 capitalizing over existing products. Part1: Principles of development and production, *Remote*
877 *Sensing of Environment*, 137, 299-309, doi:10.1016/j.rse.2012.12.027.

878 Bosilovich, M. G., et al. (2015), MERRA-2: Initial Evaluation of the ClimateRep., NASA
879 Technical Report Series on Global Modeling and Data Assimilation, NASA/TM-2015-
880 104606, Vol. 43, National Aeronautics and Space Administration, Goddard Space Flight
881 Center, Greenbelt, Maryland, USA.

882 Brown, J., O. Ferrians, J. A. Heginbottom, and E. Melnikov (2002), Circum-Arctic Map of
883 Permafrost and Ground-Ice Conditions, Version 2. [Permafrost Extent], NSIDC: National
884 Snow and Ice Data Center. Boulder, Colorado USA.

885 Camacho, F., J. Cemicharo, R. Lacaze, F. Baret, and M. Weiss (2013), GEOV1: LAI, FAPAR
886 essential climate variables and FCOVER global time series capitalizing over existing
887 products. Part 2: Validation and intercomparison with reference products, *Remote Sensing of*
888 *Environment*, 137, 310-329, doi:10.1016/j.rse.2013.02.030.

889 Carter, A., and R. Scholes (2000), SoilData v2. 0: generating a global database of soil properties,
890 *Environmentek CSIR, Pretoria, South Africa*.

891 Chen, R. H., A. Tabatabaeenejad, and M. Moghaddam (2016), A time-series active layer
892 thickness retrieval algorithm using P-and L-band SAR observations, paper presented at
893 Geoscience and Remote Sensing Symposium (IGARSS), 2016 IEEE International, IEEE.

894 De Lannoy, G. J. M., R. D. Koster, R. H. Reichle, S. P. P. Mahanama, and Q. Liu (2014), An
895 updated treatment of soil texture and associated hydraulic properties in a global land
896 modeling system, *J Adv Model Earth Sy*, 6(4), 957-979, doi:10.1002/2014ms000330.

897 Dirmeyer, P., X. Gao, and T. Oki (2002), The second global soil wetness project (gswp-2),
898 *International GEWEX Project Office Publication*, 37, 75.

899 Ducharne, A., R. D. Koster, M. J. Suarez, M. Stieglitz, and P. Kumar (2000), A catchment-based
900 approach to modeling land surface processes in a general circulation model 2. Parameter
901 estimation and model demonstration, *Journal of Geophysical Research-Atmospheres*,
902 105(D20), 24823-24838, doi:Doi 10.1029/2000jd900328.

903 Duguay, C. R., T. Zhang, D. W. Leverington, and V. E. Romanovsky (2005), Satellite remote
904 sensing of permafrost and seasonally frozen ground, *Remote Sensing in Northern Hydrology:*
905 *Measuring Environmental Change*, 91-118.

906 Farouki, O. T. (1981), The Thermal-Properties of Soils in Cold Regions, *Cold Reg Sci Technol*,
907 5(1), 67-75, doi:Doi 10.1016/0165-232x(81)90041-0.

908 Farquharson, L., D. H. Mann, G. Grosse, B. M. Jones, and V. E. Romanovsky (2016), Spatial
909 distribution of thermokarst terrain in Arctic Alaska, *Geomorphology*, 273, 116-133.

910 Frolking, S., K. McDonald, J. Kimball, S. Running, and R. Zimmermann (1999), Using the
911 space-borne NASA scatterometer (NSCAT) to determine the frozen and thawed seasons,
912 *Journal of Geophysical Research: Atmospheres*.

913 Global Modeling and Assimilation Office (GMAO) (2015a), MERRA-2 inst1_2d_lfo_Nx: 2d,1-
914 Hourly,Instantaneous,Single-Level,Assimilation,Land Surface Forcings V5.12.4, Goddard
915 Earth Sciences Data and Information Services Center (GES DISC), Accessed [03/13/2017]
916 Greenbelt, MD, USA, doi:10.5067/RCMZA6TL70BG.

917 Global Modeling and Assimilation Office (GMAO) (2015b), MERRA-2 tavg1_2d_lfo_Nx: 2d,1-
918 Hourly,Time-Averaged,Single-Level,Assimilation,Land Surface Forcings V5.12.4, Goddard
919 Earth Sciences Data and Information Services Center (GES DISC), Accessed [03/13/2017]
920 Greenbelt, MD, USA, doi:10.5067/L0T5GEG1NYFA.

921 Global Soil Data Task (2000), Global gridded surfaces of selected soil characteristics (IGBP-
922 DIS), *International Geosphere–Biosphere Programme—Data and Information Services*.
923 Available online [<http://www.daac.ornl.gov/>] from the ORNL Distributed Active Archive
924 Center, Oak Ridge National Laboratory, Oak Ridge, Tennessee, USA.

925 Hinkel, K., and F. Nelson (2003), Spatial and temporal patterns of active layer thickness at
926 Circumpolar Active Layer Monitoring (CALM) sites in northern Alaska, 1995–2000, *Journal*
927 *of Geophysical Research: Atmospheres*, 108(D2).

928 Hinzman, L. D., D. L. Kane, R. E. Gieck, and K. R. Everett (1991), Hydrologic and Thermal-
929 Properties of the Active Layer in the Alaskan Arctic, *Cold Reg Sci Technol*, 19(2), 95-110.

930 Hugelius, G., et al. (2013a), A new data set for estimating organic carbon storage to 3m depth in
931 soils of the northern circumpolar permafrost region, *Earth Syst Sci Data*, 5(2), 393-402,
932 doi:10.5194/essd-5-393-2013.

933 Hugelius, G., et al. (2014), Estimated stocks of circumpolar permafrost carbon with quantified
934 uncertainty ranges and identified data gaps, *Biogeosciences*, 11(23), 6573-6593,
935 doi:10.5194/bg-11-6573-2014.

936 Hugelius, G., C. Tarnocai, G. Broll, J. G. Canadell, P. Kuhry, and D. K. Swanson (2013b), The
937 Northern Circumpolar Soil Carbon Database: spatially distributed datasets of soil coverage
938 and soil carbon storage in the northern permafrost regions, *Earth Syst Sci Data*, 5(1), 3-13,
939 doi:10.5194/essd-5-3-2013.

940 Jafarov, E. E., S. S. Marchenko, and V. E. Romanovsky (2012), Numerical modeling of
941 permafrost dynamics in Alaska using a high spatial resolution dataset, *Cryosphere*, 6(3), 613-
942 624, doi:10.5194/tc-6-613-2012.

943 Johansen, O. (1977), Thermal conductivity of soils *Rep.*, DTIC Document, No. CRREL-TL-637.
944 COLD REGIONS RESEARCH AND ENGINEERING LAB HANOVER NH.

945 Jones, B. M., G. Grosse, C. D. Arp, M. C. Jones, K. M. W. Anthony, and V. E. Romanovsky
946 (2011), Modern thermokarst lake dynamics in the continuous permafrost zone, northern
947 Seward Peninsula, Alaska, *J Geophys Res-Biogeo*, 116, doi:10.1029/2011jg001666.

948 Kim, Y., J. S. Kimball, K. C. McDonald, and J. Glassy (2011), Developing a global data record
949 of daily landscape freeze/thaw status using satellite passive microwave remote sensing, *IEEE*
950 *Transactions on Geoscience and Remote Sensing*, 49(3), 949-960.

951 Kimball, J., K. McDonald, S. Frolking, and S. Running (2004), Radar remote sensing of the
952 spring thaw transition across a boreal landscape, *Remote Sensing of Environment*, 89(2), 163-
953 175.

954 Kimball, J., K. McDonald, A. Keyser, S. Frolking, and S. Running (2001), Application of the
955 NASA scatterometer (NSCAT) for determining the daily frozen and nonfrozen landscape of
956 Alaska, *Remote Sensing of Environment*, 75(1), 113-126.

957 Koster, R. D., and M. J. Suarez (1991), A simplified treatment of SiB's land surface albedo
958 parameterization.

959 Koster, R. D., M. J. Suarez, A. Ducharne, M. Stieglitz, and P. Kumar (2000), A catchment-based
960 approach to modeling land surface processes in a general circulation model 1. Model
961 structure, *Journal of Geophysical Research-Atmospheres*, 105(D20), 24809-24822, doi:Doi
962 10.1029/2000jd900327.

963 Koven, C. D., W. J. Riley, and A. Stern (2013), Analysis of Permafrost Thermal Dynamics and
964 Response to Climate Change in the CMIP5 Earth System Models, *Journal of Climate*, 26(6),
965 1877-1900, doi:10.1175/Jcli-D-12-00228.1.

966 Lawrence, D. M., and A. G. Slater (2005), A projection of severe near-surface permafrost
967 degradation during the 21st century, *Geophys Res Lett*, 32(24).

968 Lawrence, D. M., and A. G. Slater (2008), Incorporating organic soil into a global climate model,
969 *Clim Dynam*, 30(2-3), 145-160, doi:10.1007/s00382-007-0278-1.

970 Lawrence, D. M., A. G. Slater, V. E. Romanovsky, and D. J. Nicolsky (2008), Sensitivity of a
971 model projection of near-surface permafrost degradation to soil column depth and
972 representation of soil organic matter, *Journal of Geophysical Research-Earth Surface*,
973 113(F2), doi:10.1029/2007jf000883.

974 Liu, L., K. Schaefer, T. Zhang, and J. Wahr (2012), Estimating 1992–2000 average active layer
975 thickness on the Alaskan North Slope from remotely sensed surface subsidence, *Journal of*
976 *Geophysical Research: Earth Surface*, 117(F1).

977 Liu, L., T. Zhang, and J. Wahr (2010), InSAR measurements of surface deformation over
978 permafrost on the North Slope of Alaska, *Journal of Geophysical Research: Earth Surface*,
979 115(F3).

980 Luthin, J., and G. Guymon (1974), Soil moisture-vegetation-temperature relationships in central
981 Alaska, *J. Hydrol.*, 23(3-4), 233-246.

982 Mahanama, S. P., R. D. Koster, G. K. Walker, L. L. Takacs, R. H. Reichle, G. De Lannoy, Q.
983 Liu, B. Zhao, and M. J. Suarez (2015), Land Boundary Conditions for the Goddard Earth
984 Observing System Model Version 5 (GEOS-5) Climate Modeling System: Recent Updates
985 and Data File Descriptions.

986 Mishra, U., and W. J. Riley (2014), Active-layer thickness across Alaska: comparing
987 observation-based estimates with CMIP5 earth system model predictions, *Soil Sci Soc Am J*,
988 78(3), 894-902.

989 Molders, N., and V. E. Romanovsky (2006), Long-term evaluation of the Hydro-
990 Thermodynamic Soil-Vegetation Scheme's frozen ground/permafrost component using
991 observations at Barrow, Alaska, *Journal of Geophysical Research-Atmospheres*, 111(D4),
992 doi:10.1029/2005jd005957.

993 Moody, E. G., M. D. King, C. B. Schaaf, and S. Platnick (2008), MODIS-Derived Spatially
994 Complete Surface Albedo Products: Spatial and Temporal Pixel Distribution and Zonal
995 Averages, *Journal of Applied Meteorology and Climatology*, 47(11), 2879-2894.

996 Nelson, F., N. Shiklomanov, G. Mueller, K. Hinkel, D. Walker, and J. Bockheim (1997),
997 Estimating active-layer thickness over a large region: Kuparuk River basin, Alaska, USA,
998 *Arctic Alpine Res*, 367-378.

999 Nicolsky, D. J., V. E. Romanovsky, V. A. Alexeev, and D. M. Lawrence (2007), Improved
1000 modeling of permafrost dynamics in a GCM land-surface scheme, *Geophys Res Lett*, 34(8).

1001 Osterkamp, T. E., and V. E. Romanovsky (1999), Evidence for warming and thawing of
1002 discontinuous permafrost in Alaska, *Permafrost Periglac*, 10(1), 17-37, doi:Doi
1003 10.1002/(Sici)1099-1530(199901/03)10:1<17::Aid-Ppp303>3.0.co;2-4.

1004 Panda, S. K., A. Prakash, D. N. Solie, V. E. Romanovsky, and M. T. Jorgenson (2010), Remote
1005 Sensing and Field-based Mapping of Permafrost Distribution along the Alaska Highway
1006 Corridor, Interior Alaska, *Permafrost Periglac*, 21(3), 271-281, doi:10.1002/ppp.686.

1007 Pastick, N. J., M. T. Jorgenson, B. K. Wylie, S. J. Nield, K. D. Johnson, and A. O. Finley (2015),
1008 Distribution of near-surface permafrost in Alaska: Estimates of present and future conditions,
1009 *Remote Sensing of Environment*, 168, 301-315.

1010 Rautiainen, K., J. Lemmetyinen, M. Schwank, A. Kontu, C. B. Ménard, C. Maetzler, M. Drusch,
1011 A. Wiesmann, J. Ikonen, and J. Pulliainen (2014), Detection of soil freezing from L-band
1012 passive microwave observations, *Remote Sensing of Environment*, 147, 206-218.

1013 Reichle, R. H., G. J. M. De Lannoy, Q. Liu, J. V. Ardizzone, F. Chen, A. Colliander, A. Conaty,
1014 W. Crow, T. Jackson, J. Kimball, R. D. Koster, and E. B. Smith (2016), Soil Moisture Active
1015 Passive Mission L4_SM Data Product Assessment (Version 2 Validated Release)Rep.,
1016 NASA GMAO Office Note, No. 12 (Version 1.0), National Aeronautics and Space
1017 Administration, Goddard Space Flight Center, Greenbelt, Maryland, USA.

1018 Reichle, R. H., Q. Liu, R. D. Koster, C. S. Draper, S. P. P. Mahanama, and G. S. Partyka (2017),
1019 Land Surface Precipitation in MERRA-2, *Journal of Climate*, 30(5), 1643-1664,
1020 doi:10.1175/jcli-d-16-0570.1.

1021 Riseborough, D., N. Shiklomanov, B. Etzelmuller, S. Gruber, and S. Marchenko (2008), Recent
1022 advances in permafrost modelling, *Permafrost Periglac*, 19(2), 137-156,
1023 doi:10.1002/ppp.615.

1024 Romanovsky, V. E., A. L. Kholodov, W. L. Cable, L. Cohen, S. Panda, S. Marchenko, R. R.
1025 Muskett, and D. Nicolsky (2009), Network of Permafrost Observatories in North America
1026 and Russia. NSF Arctic Data Center, doi:10.18739/A2SH27.

1027 Romanovsky, V. E., and T. E. Osterkamp (1995), Interannual variations of the thermal regime of
1028 the active layer and near-surface permafrost in northern Alaska, *Permafrost Periglac*, 6(4),
1029 313-335, doi:DOI 10.1002/ppp.3430060404.

1030 Romanovsky, V. E., and T. E. Osterkamp (1997), Thawing of the active layer on the coastal
1031 plain of the Alaskan Arctic, *Permafrost Periglac*, 8(1), 1-22.

1032 Romanovsky, V. E., S. L. Smith, and H. H. Christiansen (2010), Permafrost Thermal State in the
1033 Polar Northern Hemisphere during the International Polar Year 2007-2009: a Synthesis,
1034 *Permafrost Periglac*, 21(2), 106-116.

1035 Sazonova, T., and V. Romanovsky (2003), A model for regional-scale estimation of temporal
1036 and spatial variability of active layer thickness and mean annual ground temperatures,
1037 *Permafrost Periglac*, 14(2), 125-139.

1038 Scholes, R., D. Skole, and J. Ingram (1995), A global database of soil properties: proposal for
1039 implementationRep., IGBP-DIS Working Paper. Report of the Global Soils Task Group,
1040 International Geosphere-Biosphere Programme - Data and Information System (IGBP-DIS).
1041 University of Paris, France.

1042 Shiklomanov, N. I., and F. E. Nelson (2002), Active-layer mapping at regional scales: A 13-year
1043 spatial time series for the Kuparuk region, north-central Alaska, *Permafrost Periglac*, 13(3),
1044 219-230.

1045 Shiklomanov, N. I., D. A. Streletskeiy, F. E. Nelson, R. D. Hollister, V. E. Romanovsky, C. E.
1046 Tweedie, J. G. Bockheim, and J. Brown (2010), Decadal variations of active-layer thickness
1047 in moisture-controlled landscapes, Barrow, Alaska, *Journal of Geophysical Research: Biogeosciences*, 115(G4).

1049 Simard, M., N. Pinto, J. B. Fisher, and A. Baccini (2011), Mapping forest canopy height globally
1050 with spaceborne lidar, *Journal of Geophysical Research: Biogeosciences*, 116(G4).

1051 Stieglitz, M., A. Ducharme, R. Koster, and M. Suarez (2001), The impact of detailed snow
1052 physics on the simulation of snow cover and subsurface thermodynamics at continental
1053 scales, *J. Hydrometeorol.*, 2(3), 228-242.

1054 Zhang, T., R. G. Barry, K. Knowles, J. Heginbottom, and J. Brown (1999), Statistics and
1055 characteristics of permafrost and ground-ice distribution in the Northern Hemisphere, *Polar
1056 Geography*, 23(2), 132-154.

1057 Zhang, T., O. W. Frauenfeld, M. C. Serreze, A. Etringer, C. Oelke, J. McCreight, R. G. Barry, D.
1058 Gilichinsky, D. Yang, and H. Ye (2005), Spatial and temporal variability in active layer
1059 thickness over the Russian Arctic drainage basin, *Journal of Geophysical Research:
1060 Atmospheres*, 110(D16).

1061 Zhao, T., L. Zhang, L. Jiang, S. Zhao, L. Chai, and R. Jin (2011), A new soil freeze/thaw
1062 discriminant algorithm using AMSR-E passive microwave imagery, *Hydrol Process*, 25(11),
1063 1704-1716.

1064 Zinke, P. J., A. G. Stangenberger, W. M. Post, W. R. Emanuel, and J. S. Olson (1986),
1065 Worldwide organic carbon and nitrogen data, *ONRL/CDIC-18, Carbon Dioxide Information
1066 Centre, Oak Ridge, Tennessee.*

1067

1068 **List of Tables**

1069	Table 1 – Land model parameters and boundary conditions.	55
1070	Table 2 – Permafrost sites used in section 5.	57
1071		

1072 **List of Figures**

1073	Figure 1 – (a) Elevation data underlying GEOS-5, (b) air temperature at 2m above the ground extracted from MERRA-2 for the Alaska domain and (c) a permafrost extent map categorized by four types, i.e., Continuous (90-100%), Discontinuous (50- 90%), sporadic(10- 50%) and isolated patches (0 - 10%) [Brown <i>et al.</i> , 2002], obtained from the National Snow and Ice Data Center. Regions in white in (a) and (b) denote glaciers. Magenta dots indicate the locations of in situ permafrost sites used in this study.	61
1079	Figure 2 – (a) Example of modeled soil temperature for 6 dates in 2014. Gray color indicates frozen soil (temperature equal to or below 273.15K). (b) 35-year climatology of frozen area, with shaded area representing the range associated with inter-annual variability. Dashed lines indicate the maximum and minimum across the 35 years.	62
1083	Figure 3 – (a) 35-year minimum, mean, and maximum of the annual ALT. The light gray color indicates permafrost-free areas. (b) Spatial mean of the annual ALT (black) and the annual mean 2-m air temperature (blue). Dashed lines are linearly fitted trend lines for the two variables.	63
1086	Figure 4 – (a) Multi-year mean of simulated (abscissa) vs. observed (ordinate) ALT. (b), (c) Maps of the multi-year mean ALT from (b) the model simulation and (c) the in situ observations.	64

1089	Figure 5 – (a) Profile-average RMSE for soil temperature estimates from the baseline simulation	
1090	at 51 sites across Alaska. (b) As in (a) but for the RMSE of each soil layer. Background shading	
1091	in (a) and (b) indicates sites that are within the same 9-km model grid cell. (c) Map of the	
1092	profile-average RMSE for soil temperature. Note that symbols overlap for sites that are close to	
1093	each other. Two overlapping areas (denoted ① and ②) are zoomed in for details.	65
1094	Figure 6 – (a) Comparison of multi-year mean seasonal cycles of observed (red) and simulated	
1095	soil temperature results at DH1 with original MERRA-2 forcing fields (in gray) and station-	
1096	based forcing (in black). Differences between simulations and observations for top four layers	
1097	are shown in panel (b).....	66
1098	Figure 7 – Comparison of observed (red) and simulated soil temperature results at UF1 with	
1099	original global land cover (denoted “Tree” in gray) and grassland (denoted “Grass” in black) in	
1100	accordance with local surface conditions. Top panel shows the observed and simulated snow	
1101	depth for each of the two experiments.....	67
1102	Figure 8 – (a) Difference of profile-average RMSE between the “Grass” experiment and the	
1103	baseline results. Blue colors (negative values) indicate model improvements whereas orange and	
1104	red colors (positive values) indicate model degradation. (b) Difference in RMSE of temperature	
1105	offset along the air-to-shallow soil gradient (Ta0) between the two experiments. (c) Difference in	
1106	RMSE of temperature offset along the shallow-to-deep soil gradient (T01) between the two	
1107	experiments.	68
1108	Figure 9 – Comparison of observed (red line) and simulated (blue line) soil temperature where	
1109	observations are used to prescribe the top layer temperature (denoted T1BC) at UF1 and SL1.	
1110	For SL1, simulation results from T2BC (green line) in which soil temperatures at both the 1 st and	
1111	the 2 nd layer were prescribed to observations are also shown.	69

1112	Figure 10 – (a) Vertical profiles of soil carbon fraction (fsc) based on IGBP-DIS and NCSCD at	
1113	sites FB1, GL1, SG2 and SL2. Profiles at SL1, SL3 and SL4 are identical to SL2. The gray	
1114	profile is based on IGBP-DIS. The black dash profile is derived using NCSCD. The cumulative	
1115	carbon storage profile for polar and boreal soils as identified in <i>Zinke et al. [1986]</i> was used to	
1116	calculate the vertical profile. (b) Example of the associated soil thermal properties at site GL1,	
1117	including the thermal conductivity for soil solids (λ_s), the thermal conductivity for dry soil	
1118	(λ_{dry}), the specific heat capacity of soil (cs) and soil porosity. Blue line represents the default	
1119	values originally used in CLSM. Cyan shading indicates the extent of the top two model layers.	
1120	70
1121	Figure 11 – Simulation results at GL1 and SL2 for baseline T1BC experiment in which soil	
1122	temperature in the top layer was prescribed from in situ observations, as well as from two T1BC	
1123	simulations (T1BC_OrgC_IBGP and T1BC_OrgC_NCSCD) that incorporate organic carbon	
1124	content profiles derived from the two carbon datasets (IGBP-DIS and NCSCD).....	71
1125	Figure 12 – RMSE ($^{\circ}$ C) of soil temperature for individual model layers and the profile-average	
1126	RMSE (PfAvg) at FB1, GL1, SG2, SL2, SL3, SL4, and SL1 from the baseline T1BC simulation	
1127	and from the two T1BC simulations incorporating organic carbon content profiles	
1128	(T1BC_OrgC_IBGP and T1BC_OrgC_NCSCD). For SL1, RMSEs for the baseline T2BC	
1129	simulation and from the two T2BC simulations using the carbon datasets are also shown.	72
1130	Figure 13 – The RMSEs of annual ALT from different experiments at the seven testing sites,	
1131	including three simulations with MERRA-2 forcing (i.e. Baseline, M2_OrgC_IBGP and	
1132	M2_OrgC_NCSCD) and three simulations with prescribed top soil temperature (i.e. T1BC,	
1133	T1BC_OrgC_IBGP and T1BC_OrgC_NCSCD). Baseline simulation results indicate that SL1,	
1134	SL2, SL3 and SL4 are all permafrost free and thus the RMSE for these sites are null.	73

1135 Figure 14 – (a) Multi-year mean of estimated ALT from three simulations driven by MERRA2
1136 forcing vs. observed ALT at sites across Alaska, including baseline simulation and the two
1137 simulations incorporating organic carbon impacts (M2_OrgC_IBGP and M2_OrgC_NCSCD).
1138 Open cycles represent sites that baseline simulation show permafrost-free (thus no corresponding
1139 green dots) whereas the simulations with carbon impacts do not, and are not used for calculation
1140 of RMSE and bias. (b) RMSE of the multi-year mean of ALT from the three experiments. (c)
1141 Mean of bias of the multi-year mean of ALT from the three experiments..... 74

1142

1143

1144 Table 1 – Land model parameters and boundary conditions.

Land boundary conditions	Data source or generation method	Reference
Soil Depth	The Second Global Soil Wetness Project (GSWP-2).	[Dirmeyer <i>et al.</i> , 2002]
Soil parameters	Harmonized World Soil Data (HWSD-1.21) and the State Soil Geographic (STATSGO2) data set.	[De Lannoy <i>et al.</i> , 2014]
Land cover	USGS Global Land Cover Characteristics Data Base Version 2.0 (GLCCv2).	https://lta.cr.usgs.gov/glcc/
Vegetation height	The Geoscience Laser Altimeter System (GLAS) aboard ICESat (Ice, Cloud, and land Elevation Satellite).	[Simard <i>et al.</i> , 2011]
Leaf Area Index (LAI)	Moderate Resolution Imaging Spectroradiometer (MODIS) and GEOLAND2 LAI product.	[Baret <i>et al.</i> , 2013; Camacho <i>et al.</i> , 2013]
Greenness fraction	GSWP-2	[Dirmeyer <i>et al.</i> , 2002]
Albedo	Computed by a modified Simple Biosphere	[Koster and Suarez, 1991;

	Model (SiB) albedo parameterization scheme and (for the snow-free fraction) scaled by MODIS albedo climatology.	<i>Moody et al., 2008]</i>
--	---	----------------------------

1145

1146

1147 Table 2 – Permafrost sites used in Section 5.

Permafrost Sites	Latitude	Longitude	Local landcover*	Local soil information#	Purpose
DH1	70.1613°	-148.4653°	Landcover units include Graminoid-moss tundra and graminoid, prostrate-dwarf-shrub, moss tundra (wet and moist nonacidic).	15cm - Peat.	Examining Meteorological Forcing (section 5.1)
FB1	69.6739°	-148.7219°	Landcover units include Graminoid-moss tundra and graminoid, prostrate-dwarf-shrub, moss tundra (wet and moist nonacidic). This site is located on	15cm – Peat.	Examining upper boundary condition and soil organic carbon content (section 5.4)

			the inner coastal plain with river terraces.		
GL1	68.4774°	-149.5024°	Landcover units include Graminoid-moss tundra and graminoid, prostrate-dwarf-shrub, moss tundra (wet and moist nonacidic). Broad glaciated mountain valley.	80cm – Peat; 127cm - Silty loam; 199cm - Peat and silt mix; 278cm – silt.	Examining upper boundary condition and soil organic carbon content (section 5.4)
SG2	69.4283°	-148.7001°	Moist acidic tundra	15cm – Peat; 40cm - Silty loam.	Examining upper boundary condition and soil organic carbon content (section 5.4)
SL1	64.8694°	-147.8608°	Forest	31cm – Peat.	Examining upper boundary

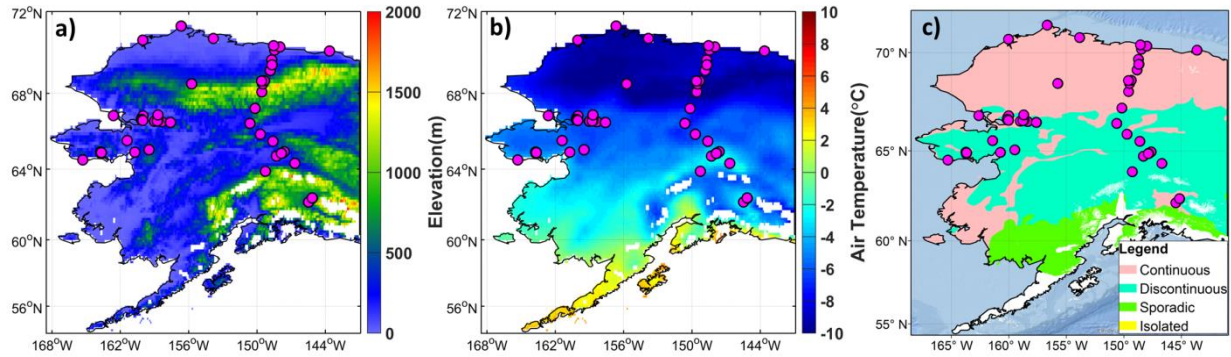
					condition and soil organic carbon content (section 5.3 and 5.4)
SL2	64.8661°	-147.8568°	Forest	---	Examining upper boundary condition and soil organic carbon content (section 5.4)
SL3	64.8675°	-147.8588°	Forest	---	Examining upper boundary condition and soil organic carbon content (section 5.4)
SL4	64.8669°	-147.8584°	Forest	---	Examining upper boundary condition and soil organic carbon content (section

					5.4)
UF1	64.8529°	-147.8575°	Agricultural field	---	Examining land cover type and upper boundary condition (section 5.2 and 5.3)

1148 * Information is from http://permafrost.gi.alaska.edu/sites_map.

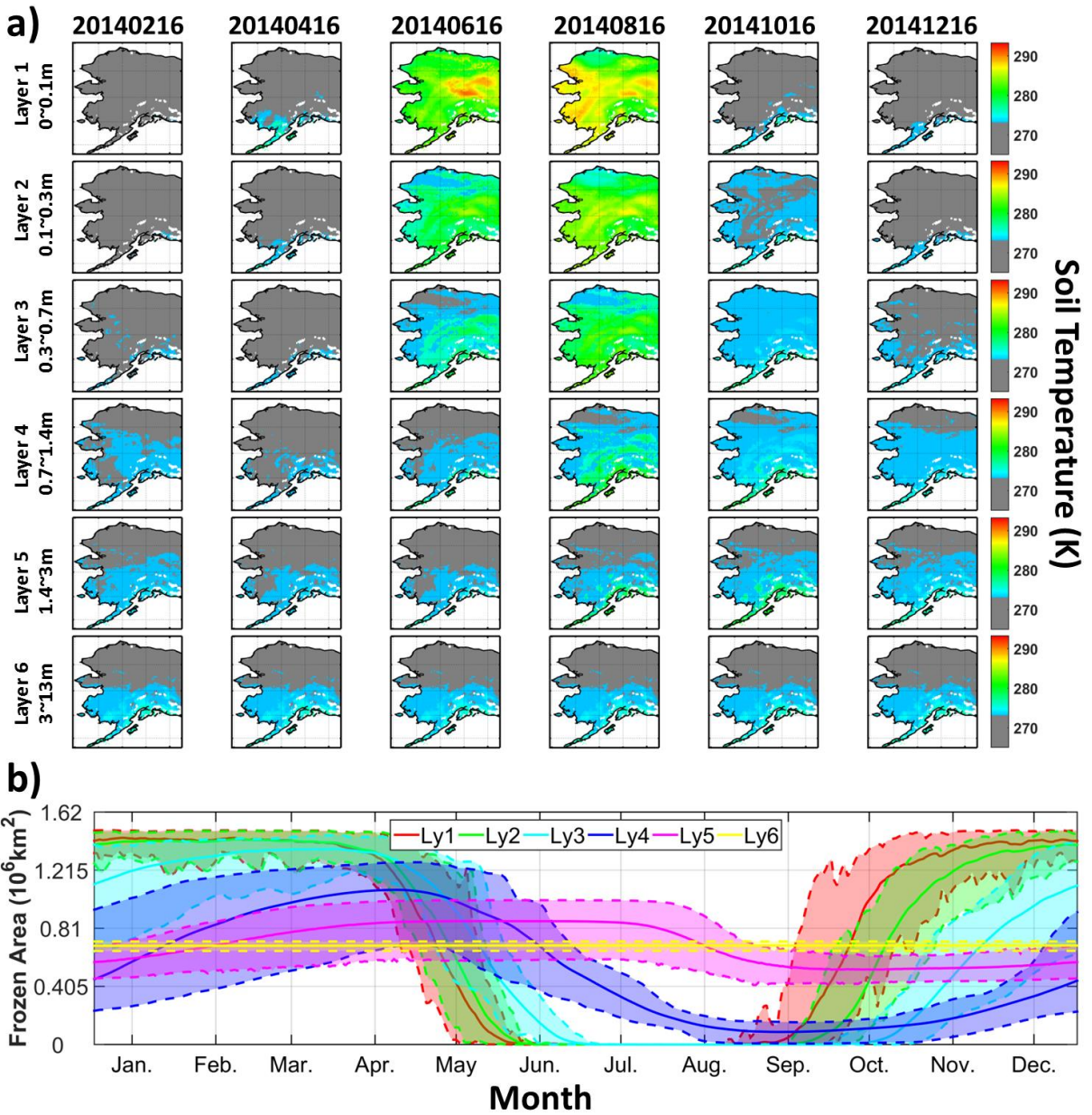
1149 # Information is from personal communication with Dr. Vladimir Romanovsky and Dr.

1150 Alexander Kholodov from University of Alaska Fairbanks.



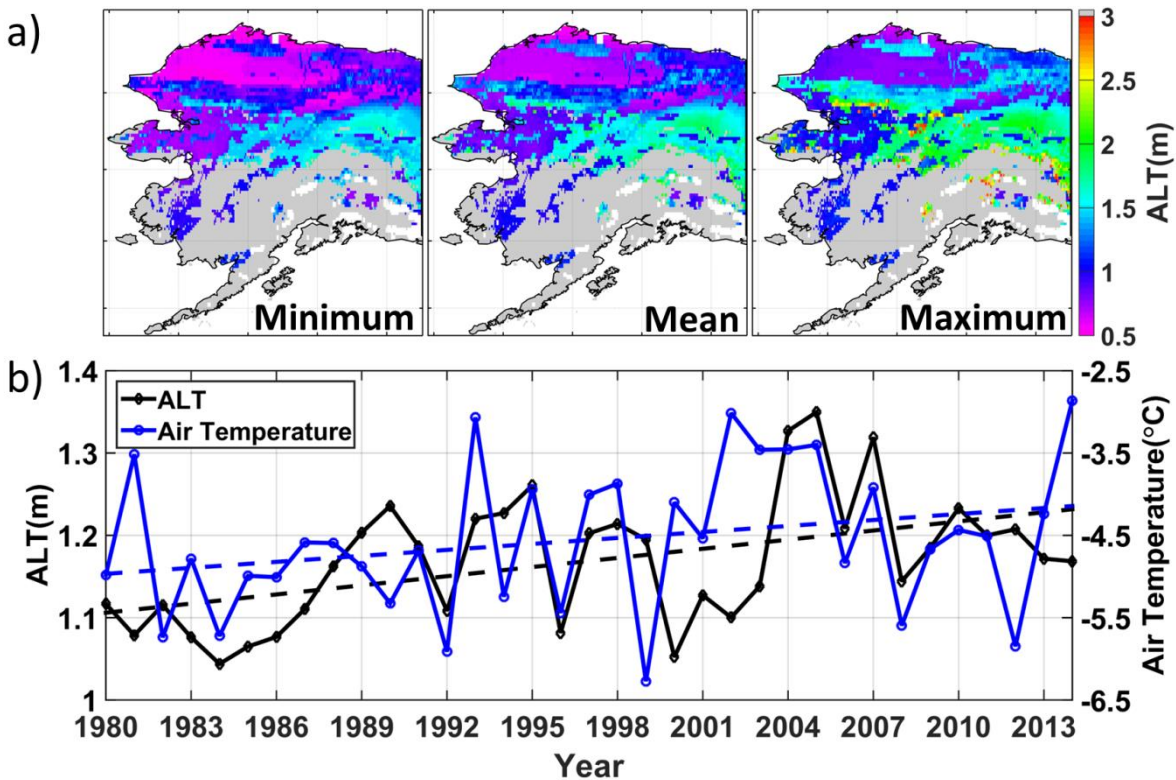
1151
1152 Figure 1 – (a) Elevation data underlying GEOS-5, (b) air temperature at 2m above the ground
1153 extracted from MERRA-2 for the Alaska domain and (c) a permafrost extent map categorized by
1154 four types, i.e., Continuous (90-100%), Discontinuous (50- 90%), sporadic(10- 50%) and
1155 isolated patches (0 - 10%) [Brown *et al.*, 2002], obtained from the National Snow and Ice Data
1156 Center. Regions in white in (a) and (b) denote glaciers. Magenta dots indicate the locations of in
1157 situ permafrost sites used in this study.

1158



1159

1160 Figure 2 – (a) Example of modeled soil temperature for 6 dates in 2014. Gray color indicates
 1161 frozen soil (temperature equal to or below 273.15K). (b) 35-year climatology of frozen area,
 1162 with shaded area representing the range associated with inter-annual variability. Dashed lines
 1163 indicate the maximum and minimum across the 35 years.

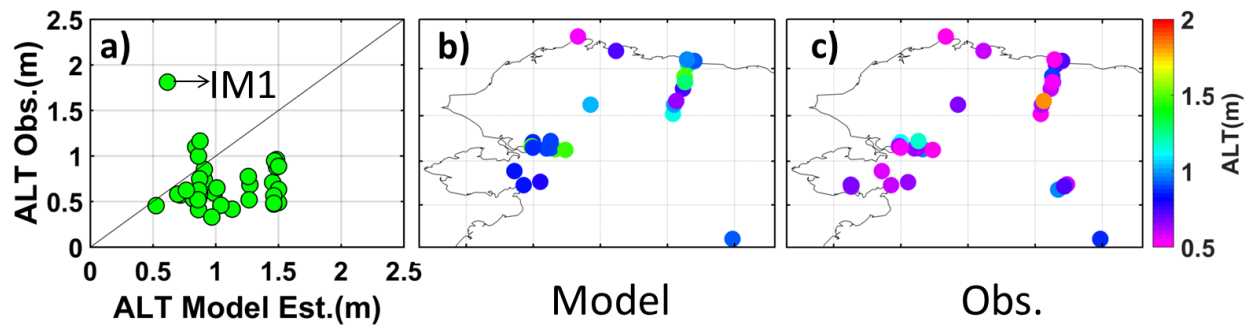


1164

1165 Figure 3 – (a) 35-year minimum, mean, and maximum of the annual ALT. The light gray color
 1166 indicates permafrost-free areas. (b) Spatial mean of the annual ALT (black) and the annual mean
 1167 2-m air temperature (blue). Dashed lines are linearly fitted trend lines for the two variables.

1168

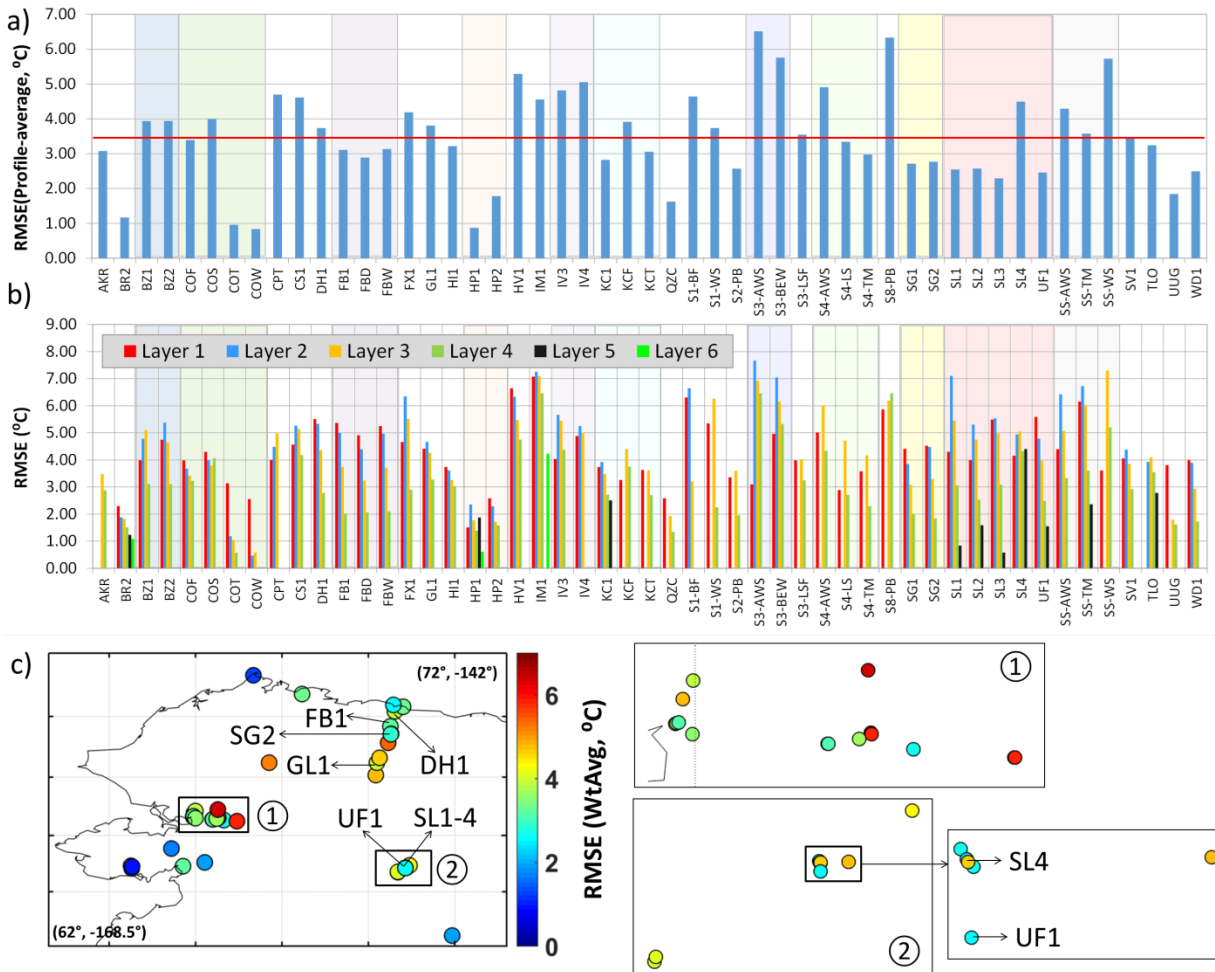
1169



1170

1171 Figure 4 – (a) Multi-year mean of simulated (abscissa) vs. observed (ordinate) ALT. (b), (c)
 1172 Maps of the multi-year mean ALT from (b) the model simulation and (c) the in situ observations.

1173

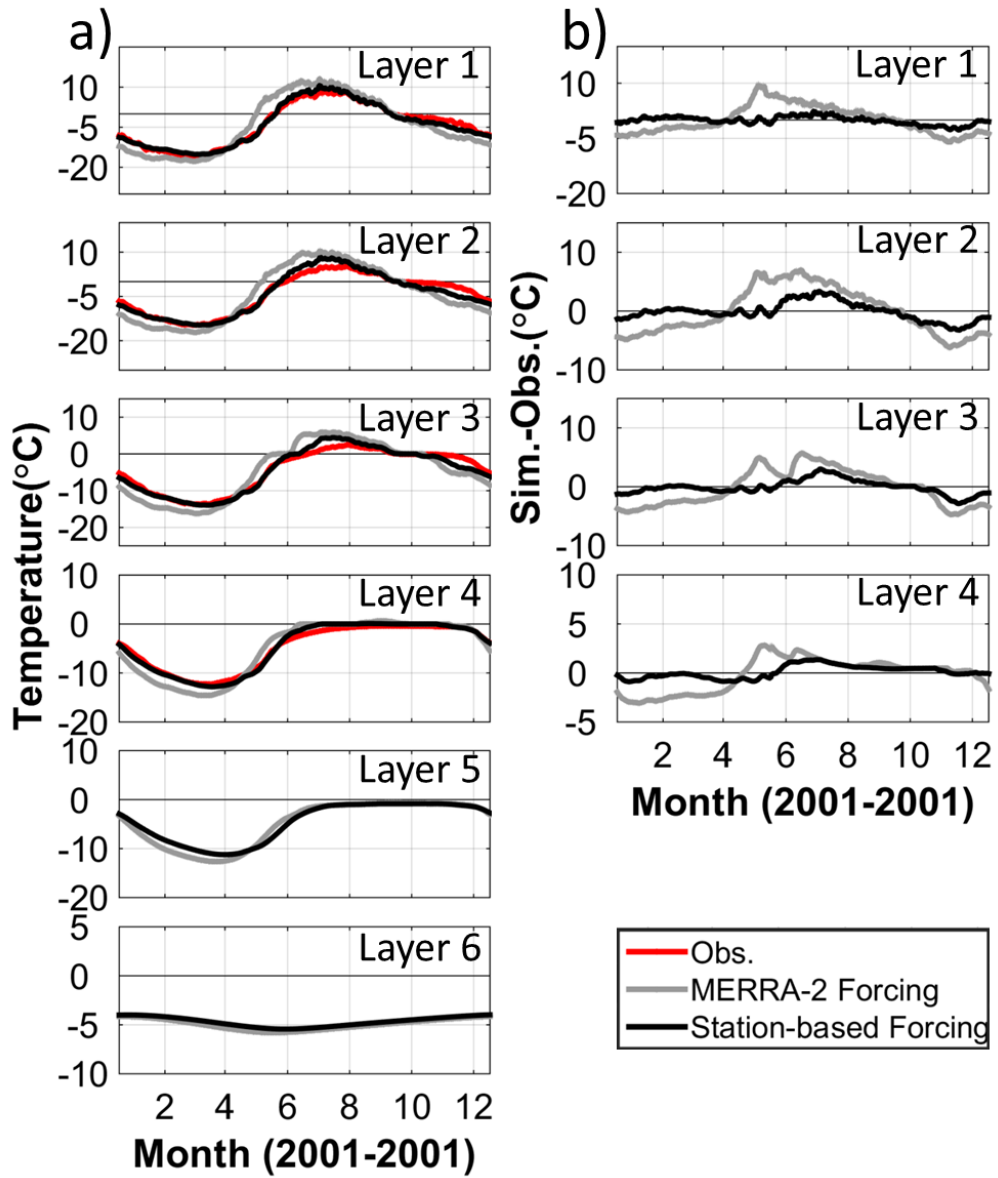


1174

1175 Figure 5 – (a) Profile-average RMSE for soil temperature estimates from the baseline simulation
 1176 at 51 sites across Alaska. (b) As in (a) but for the RMSE of each soil layer. Background shading
 1177 in (a) and (b) indicates sites that are within the same 9-km model grid cell. (c) Map of the
 1178 profile-average RMSE for soil temperature. Note that symbols overlap for sites that are close to
 1179 each other. Two overlapping areas (denoted ① and ②) are zoomed in for details.

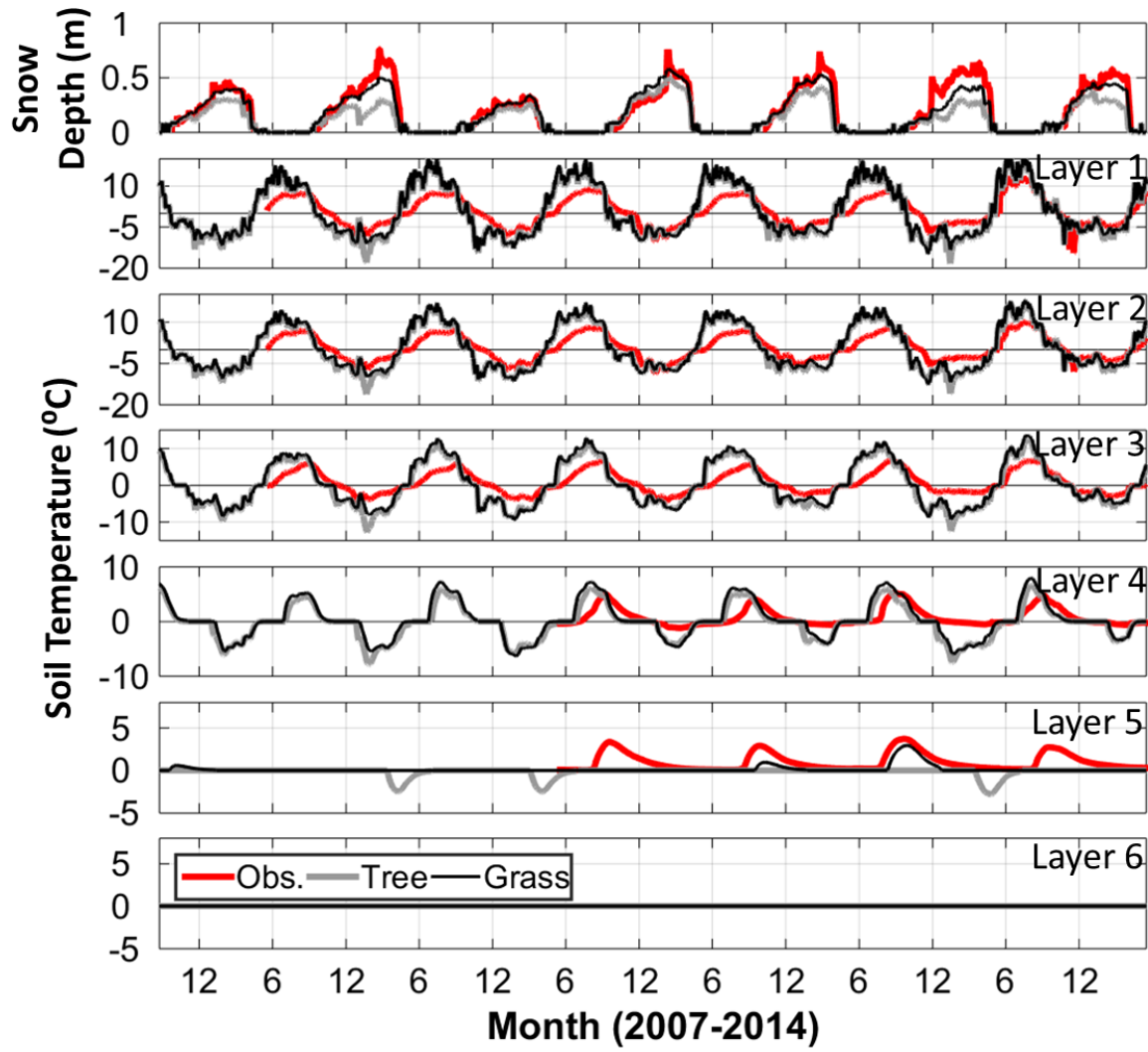
1180

1181



1182

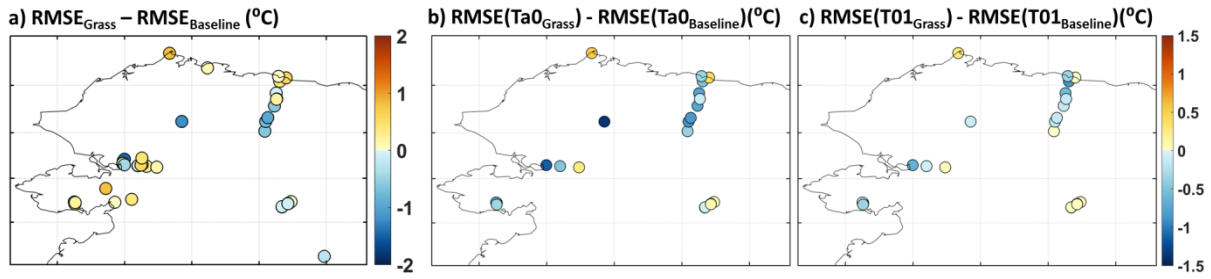
1183 Figure 6 – (a) Comparison of multi-year mean seasonal cycles of observed (red) and simulated
 1184 soil temperature results at DH1 with original MERRA-2 forcing fields (in gray) and station-
 1185 based forcing (in black). Differences between simulations and observations for top four layers
 1186 are shown in panel (b).



1187

1188 Figure 7 – Comparison of observed (red) and simulated soil temperature results at UF1 with
 1189 original global land cover (denoted “Tree” in gray) and grassland (denoted “Grass” in black) in
 1190 accordance with local surface conditions. Top panel shows the observed and simulated snow
 1191 depth for each of the two experiments.

1192

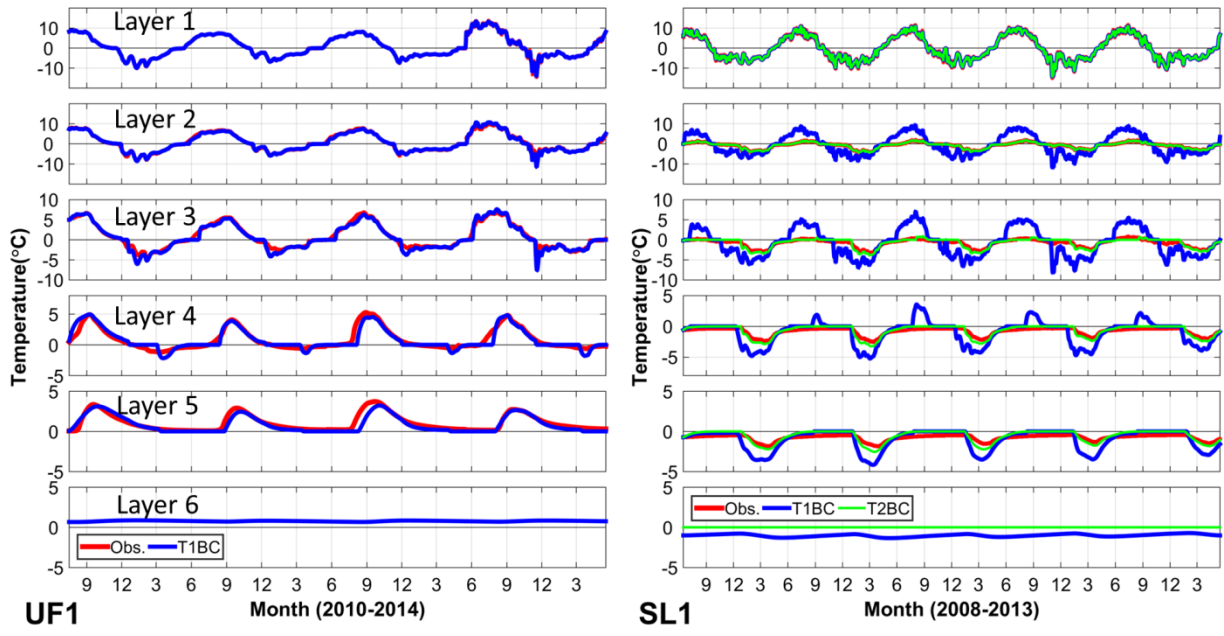


1193

1194 Figure 8 – (a) Difference of profile-average RMSE between the “Grass” experiment and the
 1195 baseline results. Blue colors (negative values) indicate model improvements whereas orange and
 1196 red colors (positive values) indicate model degradation. (b) Difference in RMSE of temperature
 1197 offset along the air-to-shallow soil gradient (Ta0) between the two experiments. (c) Difference in
 1198 RMSE of temperature offset along the shallow-to-deep soil gradient (T01) between the two
 1199 experiments.

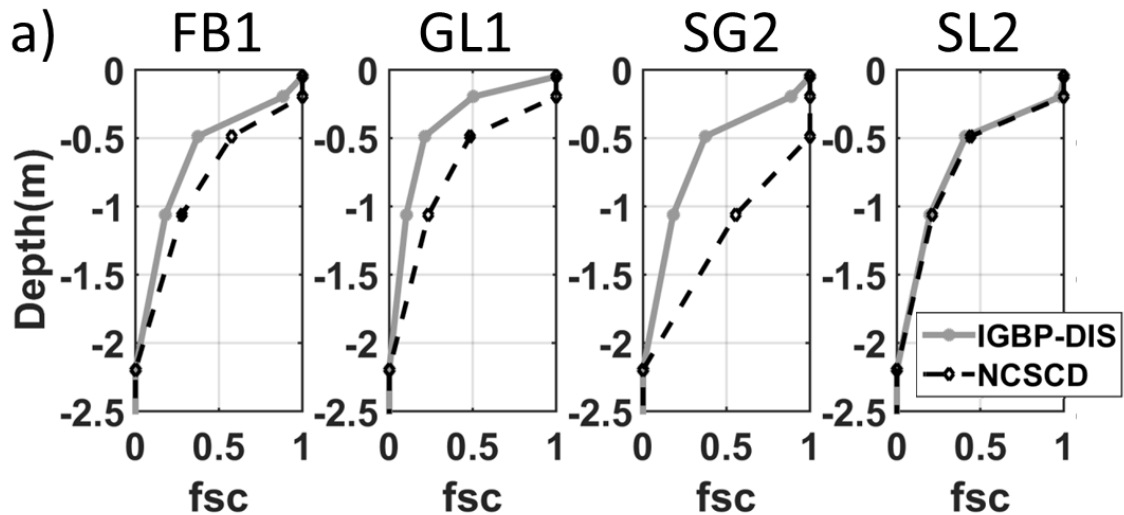
1200

1201

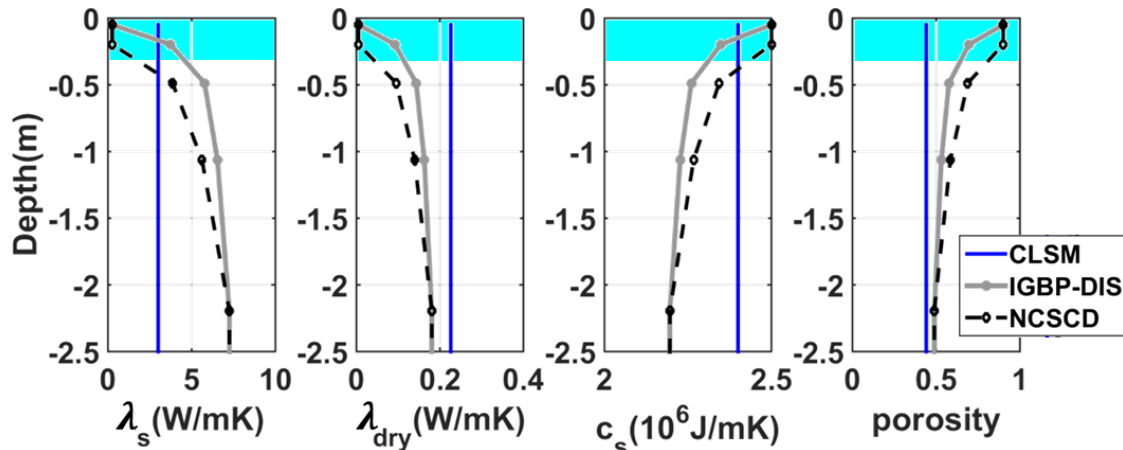


1202

1203 Figure 9 – Comparison of observed (red line) and simulated (blue line) soil temperature where
 1204 observations are used to prescribe the top layer temperature (denoted T1BC) at UF1 and SL1.
 1205 For SL1, simulation results from T2BC (green line) in which soil temperatures at both the 1st and
 1206 the 2nd layer were prescribed to observations are also shown.

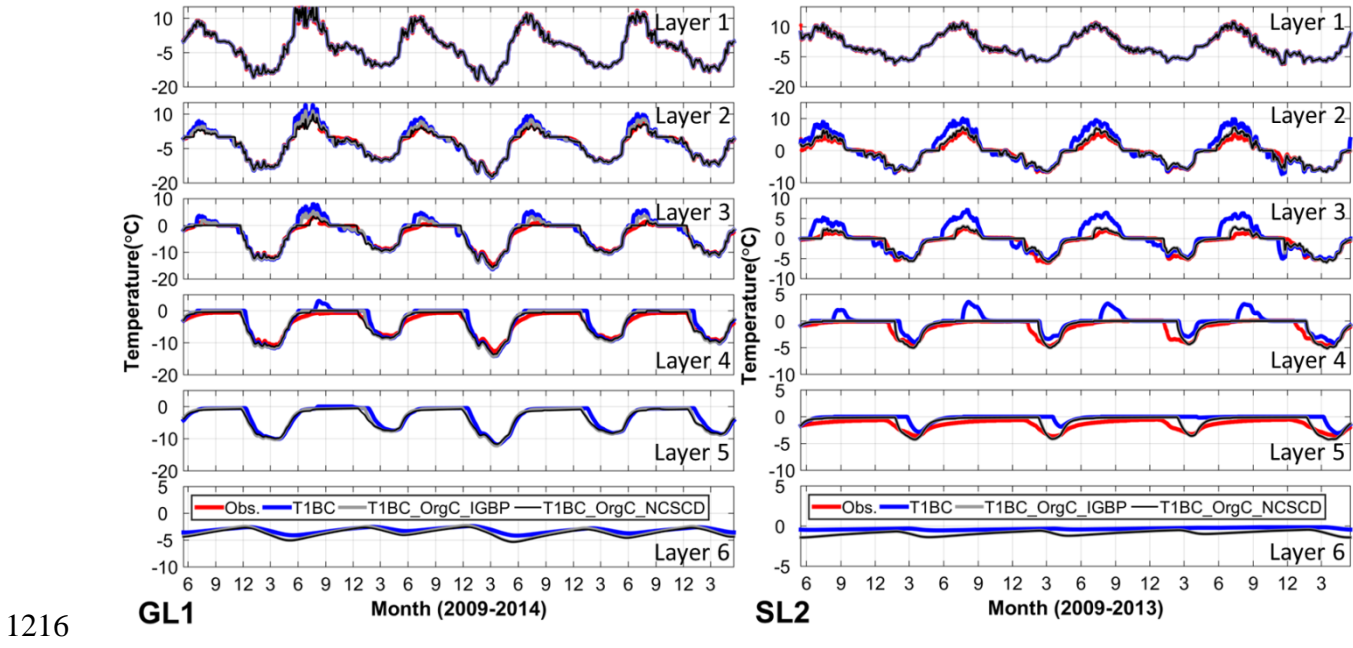


b) Soil thermal properties at GL1



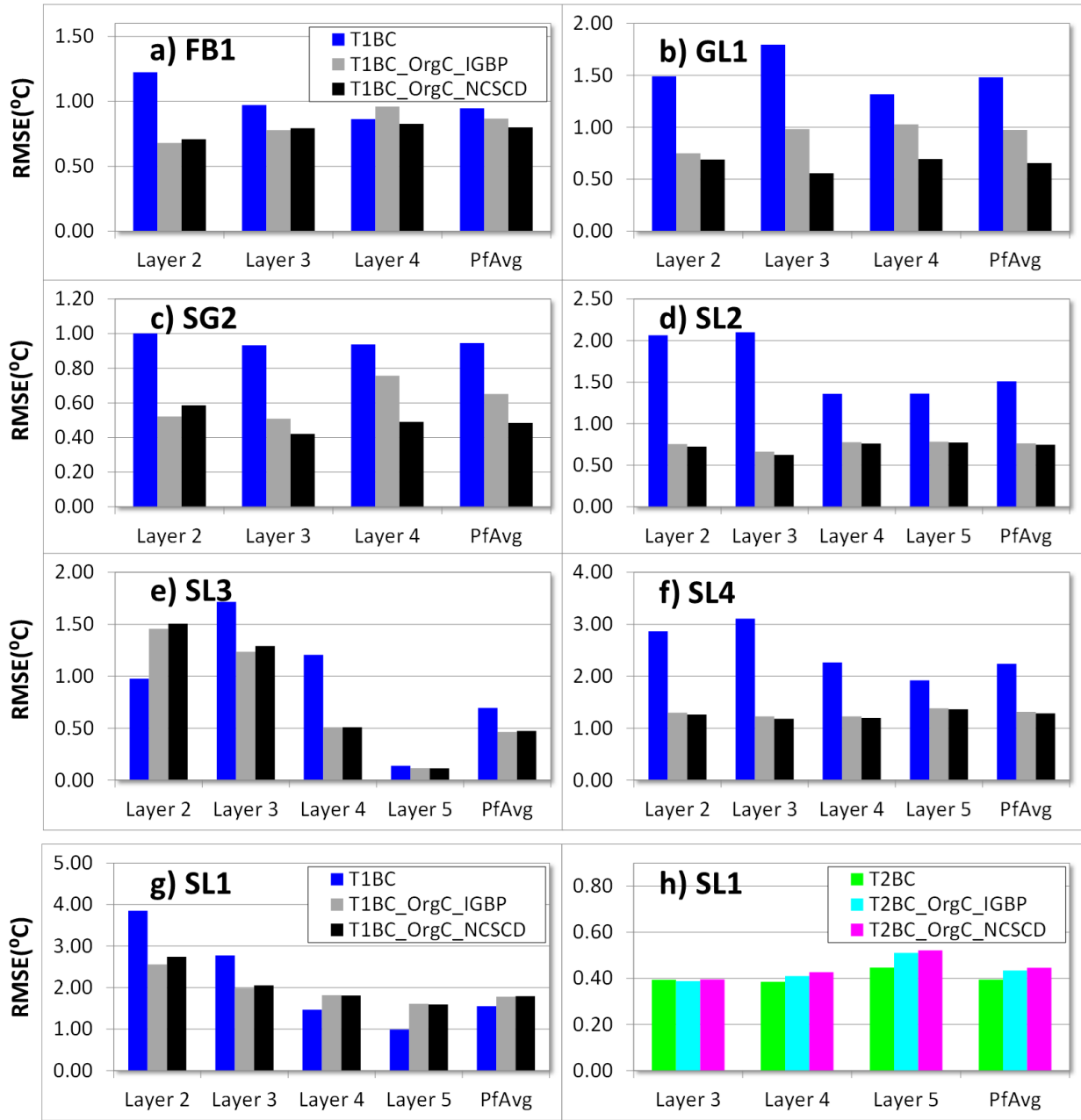
1207

Figure 10 – (a) Vertical profiles of soil carbon fraction (fsc) based on IGBP-DIS and NCSCD at sites FB1, GL1, SG2 and SL2. Profiles at SL1, SL3 and SL4 are identical to SL2. The gray profile is based on IGBP-DIS. The black dash profile is derived using NCSCD. The cumulative carbon storage profile for polar and boreal soils as identified in *Zinke et al. [1986]* was used to calculate the vertical profile. (b) Example of the associated soil thermal properties at site GL1, including the thermal conductivity for soil solids (λ_s), the thermal conductivity for dry soil (λ_{dry}), the specific heat capacity of soil (c_s) and soil porosity. Blue line represents the default values originally used in CLSM. Cyan shading indicates the extent of the top two model layers.



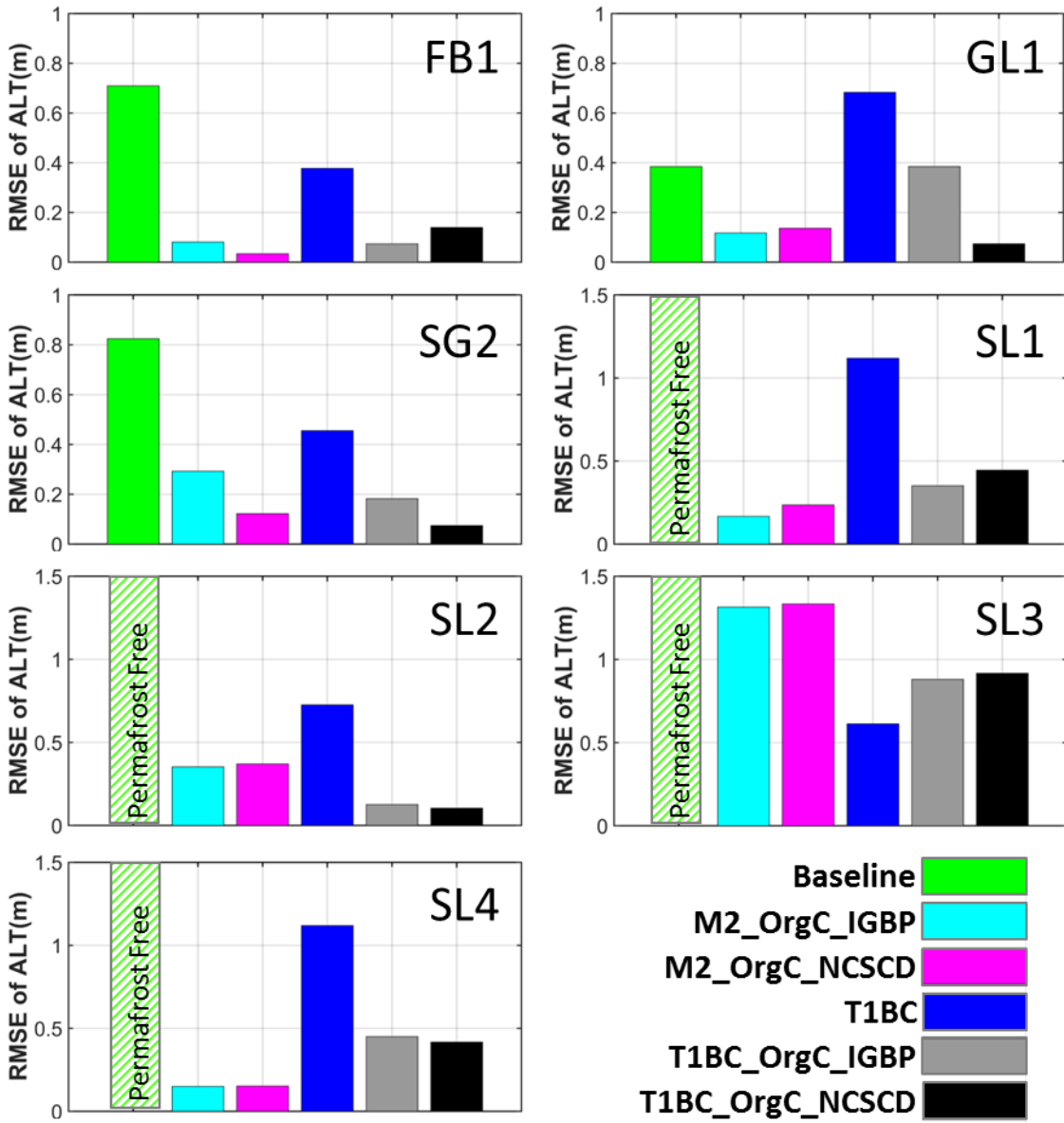
1217 Figure 11 – Simulation results at GL1 and SL2 for baseline T1BC experiment in which soil
 1218 temperature in the top layer was prescribed from in situ observations, as well as from two T1BC
 1219 simulations (T1BC_OrgC_IBGP and T1BC_OrgC_NCSCD) that incorporate organic carbon
 1220 content profiles derived from the two carbon datasets (IGBP-DIS and NCSCD).

1221



1222

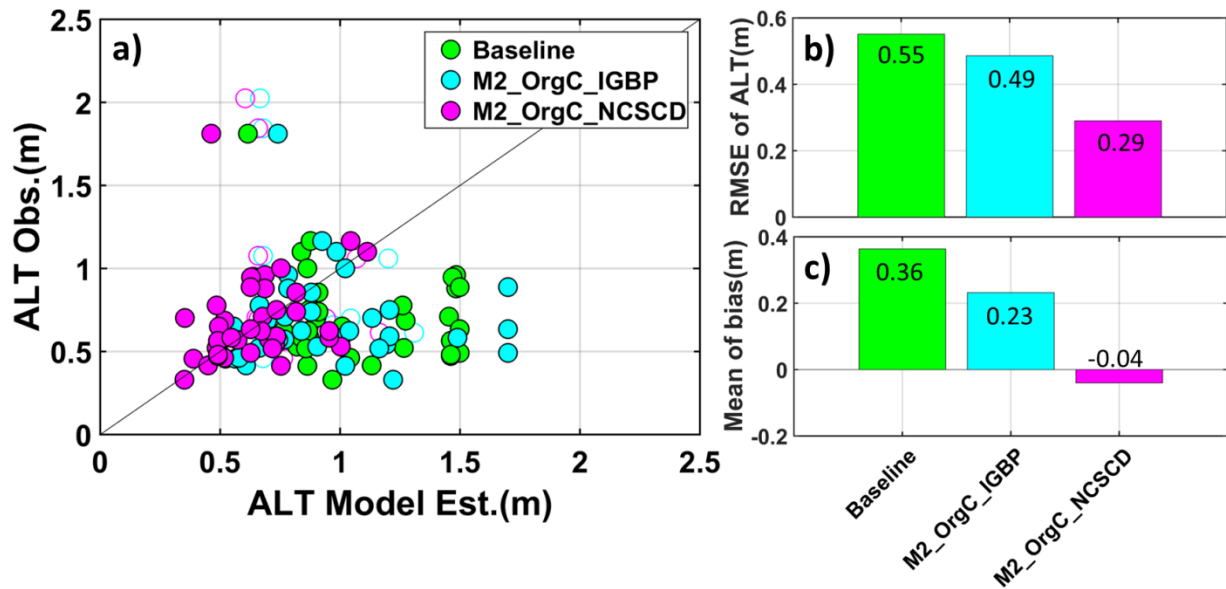
1223 Figure 12 – RMSE (°C) of soil temperature for individual model layers and the profile-average
 1224 RMSE (PfAvg) at FB1, GL1, SG2, SL2, SL3, SL4, and SL1 from the baseline T1BC simulation
 1225 and from the two T1BC simulations incorporating organic carbon content profiles
 1226 (T1BC_OrgC_IGBP and T1BC_OrgC_NCSND). For SL1, RMSEs for the baseline T2BC
 1227 simulation and from the two T2BC simulations using the carbon datasets are also shown.



1228

1229 Figure 13 – The RMSEs of annual ALT from different experiments at the seven testing sites,
1230 including three simulations with MERRA-2 forcing (i.e. Baseline, M2_OrgC_IBGP and
1231 M2_OrgC_NCSCD) and three simulations with prescribed top soil temperature (i.e. T1BC,
1232 T1BC_OrgC_IBGP and T1BC_OrgC_NCSCD). Baseline simulation results indicate that SL1,
1233 SL2, SL3 and SL4 are all permafrost free and thus the RMSE for these sites are null.

1234



1235

1236 Figure 14 – (a) Multi-year mean of estimated ALT from three simulations driven by MERRA2
 1237 forcing vs. observed ALT at sites across Alaska, including baseline simulation and the two
 1238 simulations incorporating organic carbon impacts (M2_OrgC_IBGP and M2_OrgC_NCSCD).
 1239 Open cycles represent sites that baseline simulation show permafrost-free (thus no corresponding
 1240 green dots) whereas the simulations with carbon impacts do not, and are not used for calculation
 1241 of RMSE and bias. (b) RMSE of the multi-year mean of ALT from the three experiments. (c)
 1242 Mean of bias of the multi-year mean of ALT from the three experiments.

Figure 1.

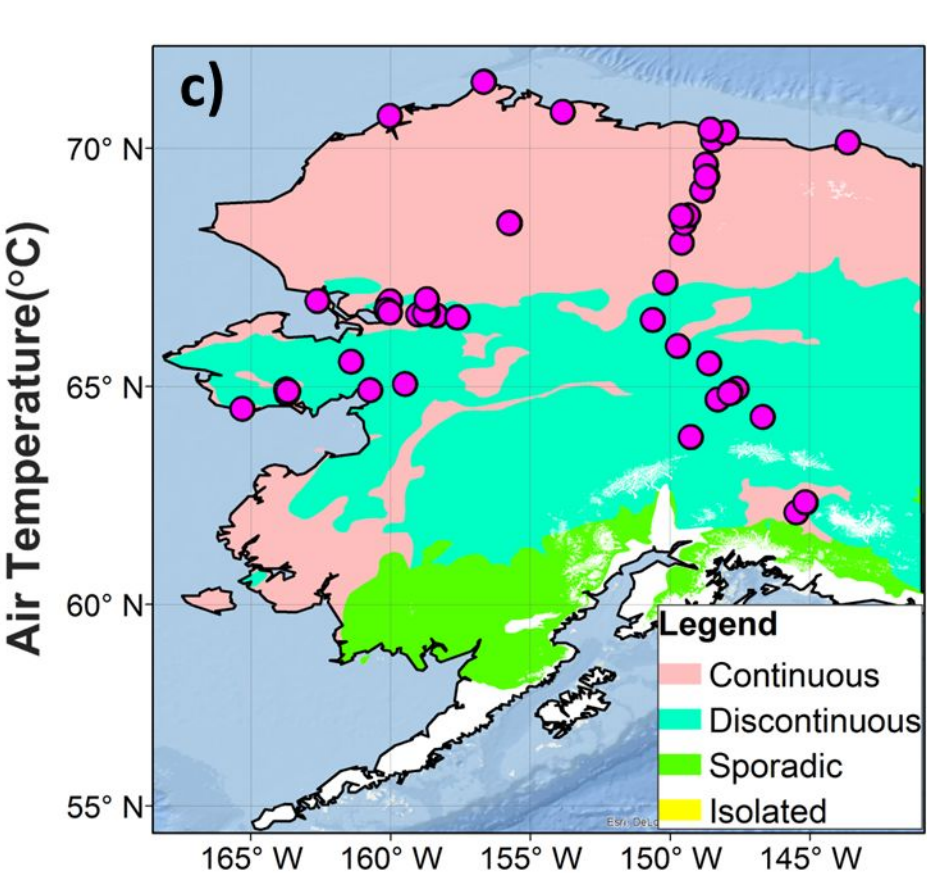
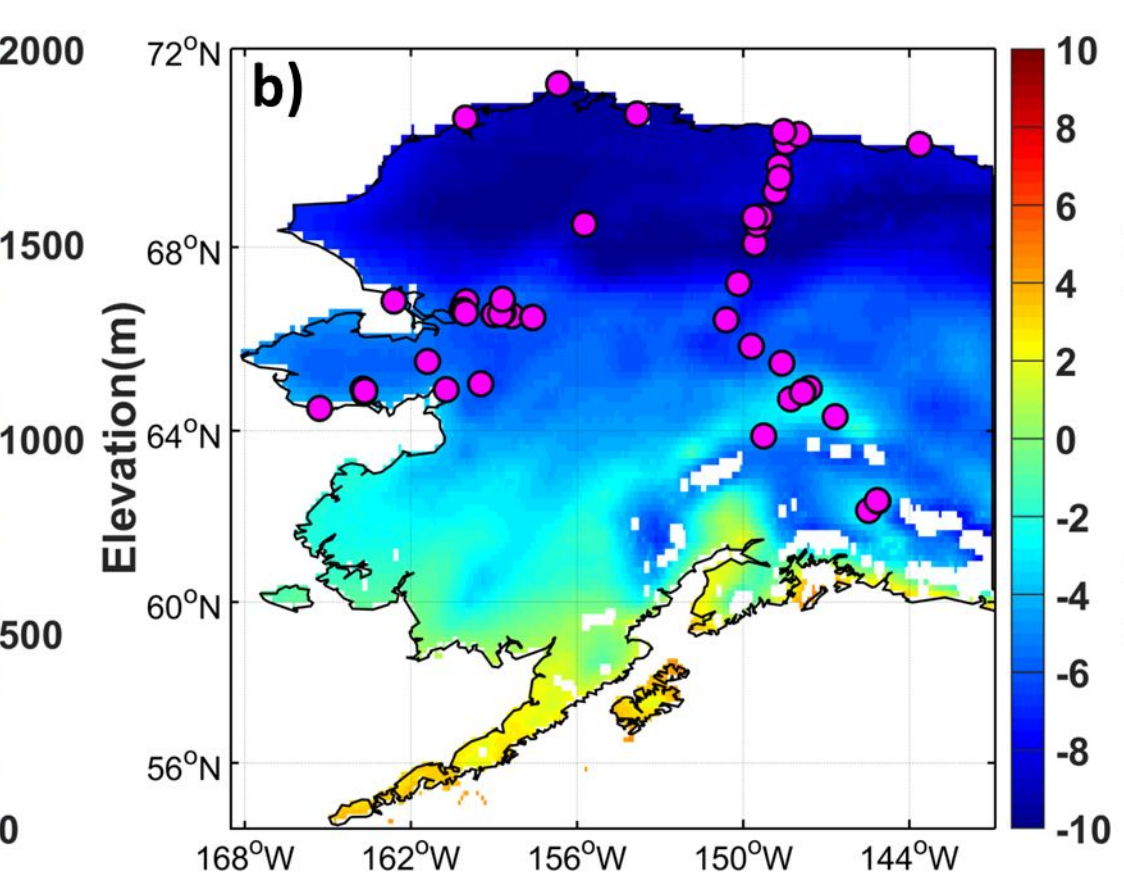
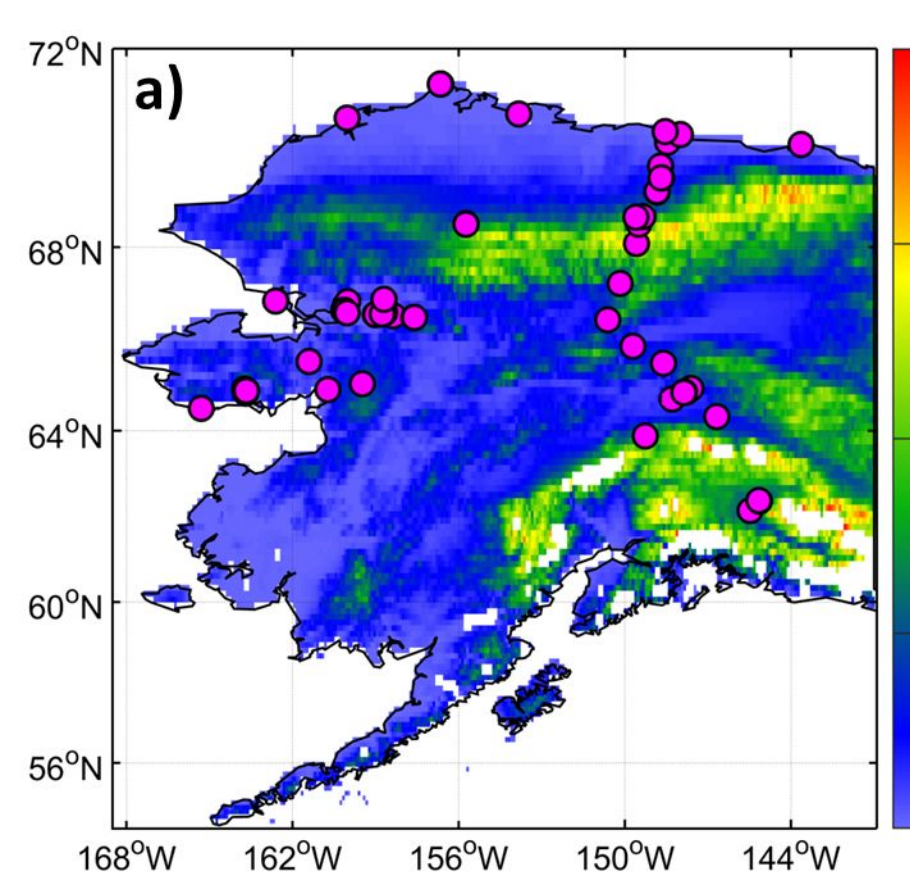


Figure 2.

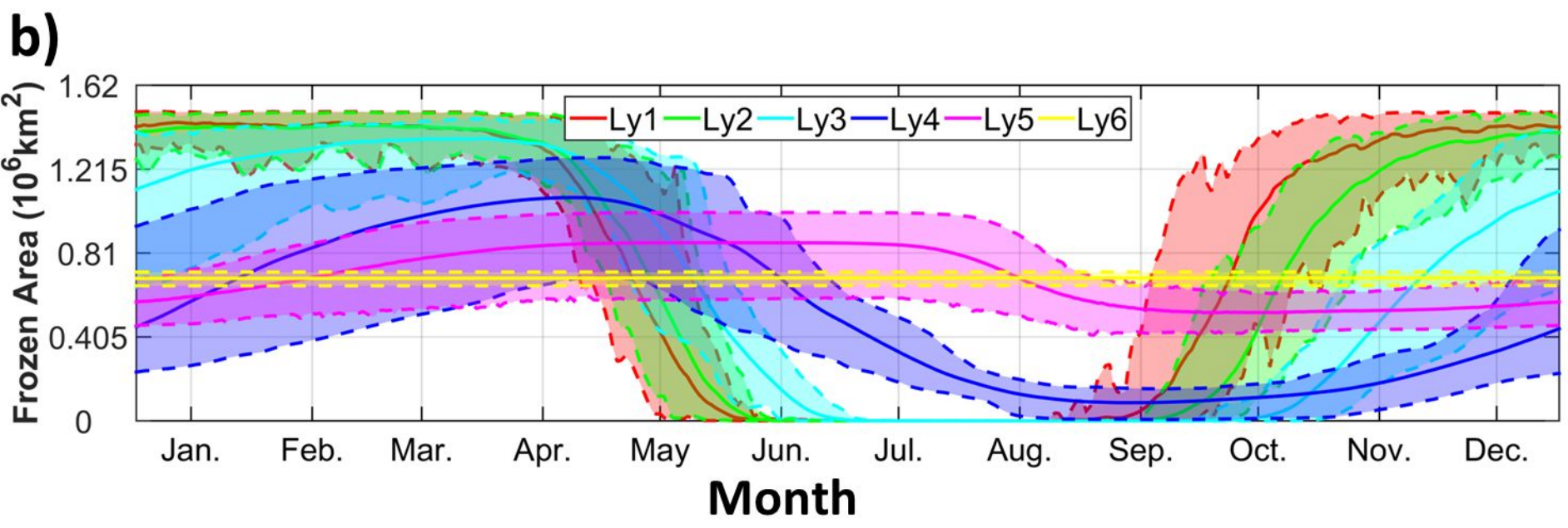
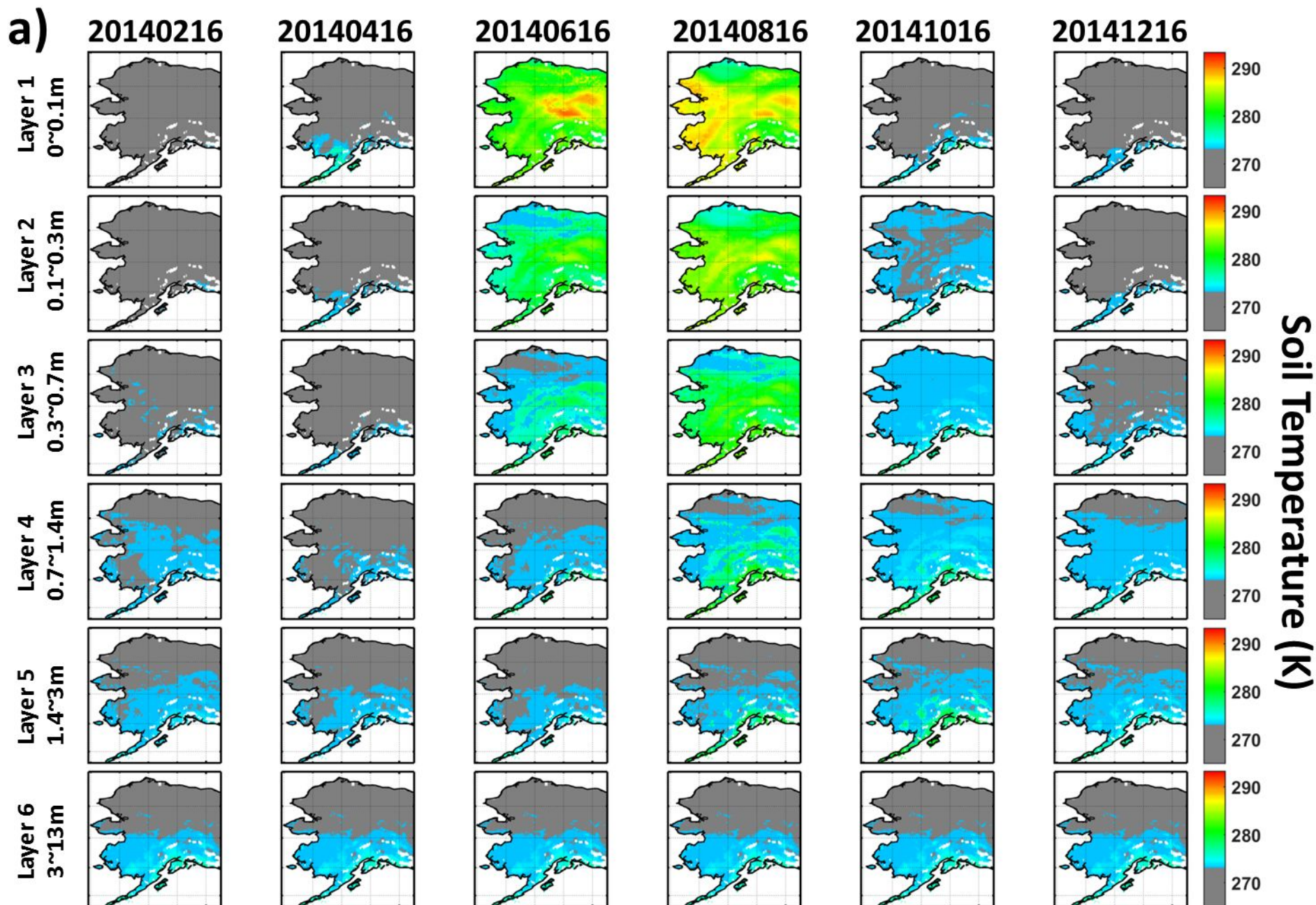


Figure 3.

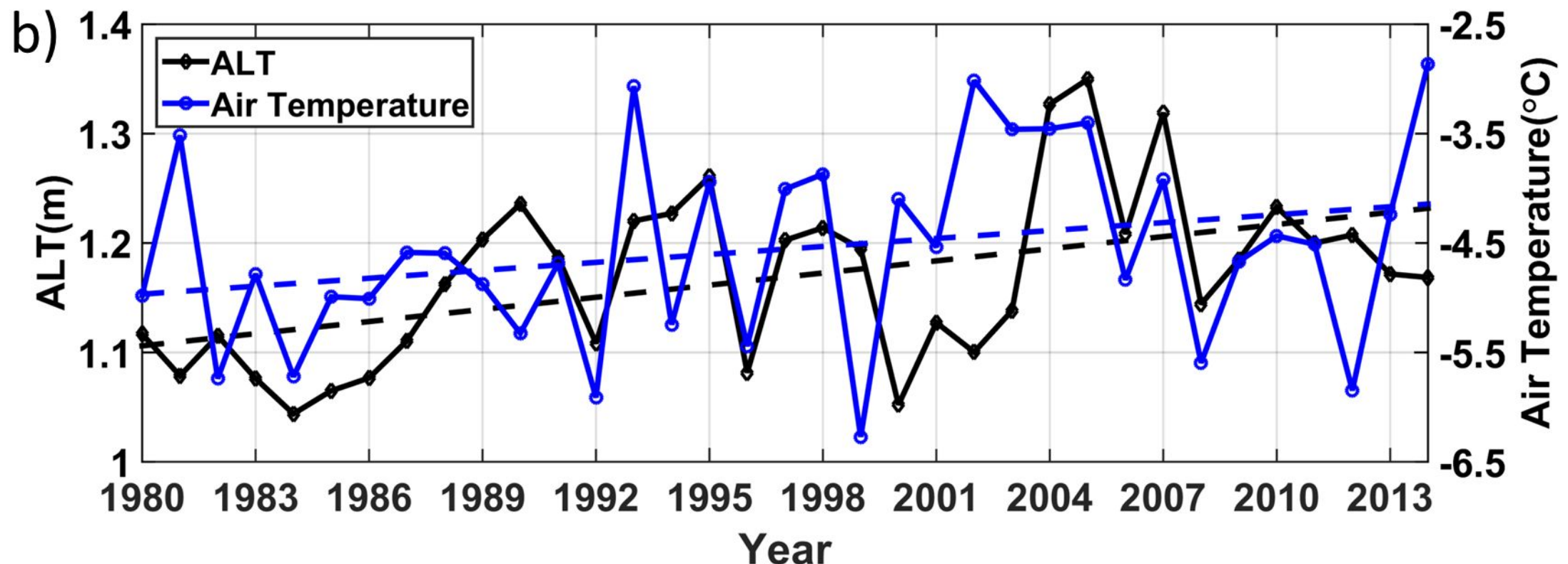
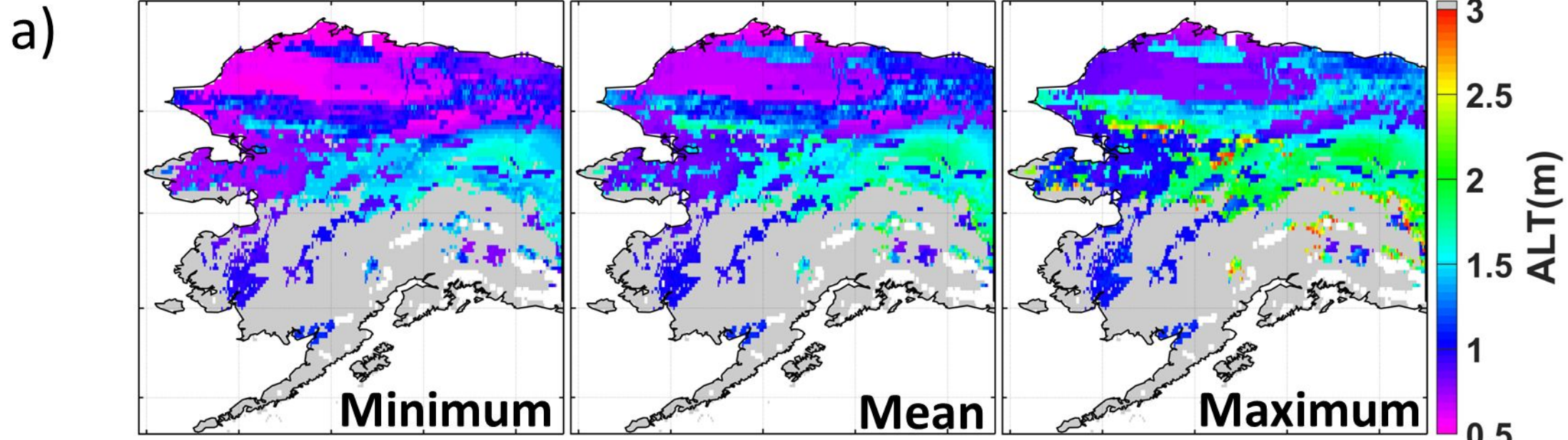


Figure 4.

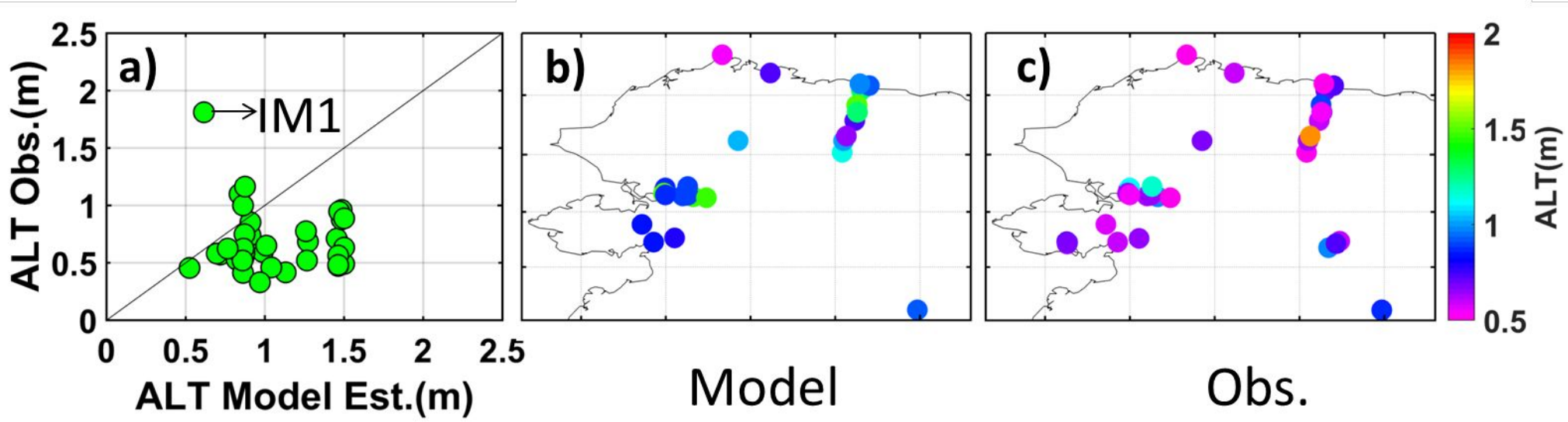


Figure 5.

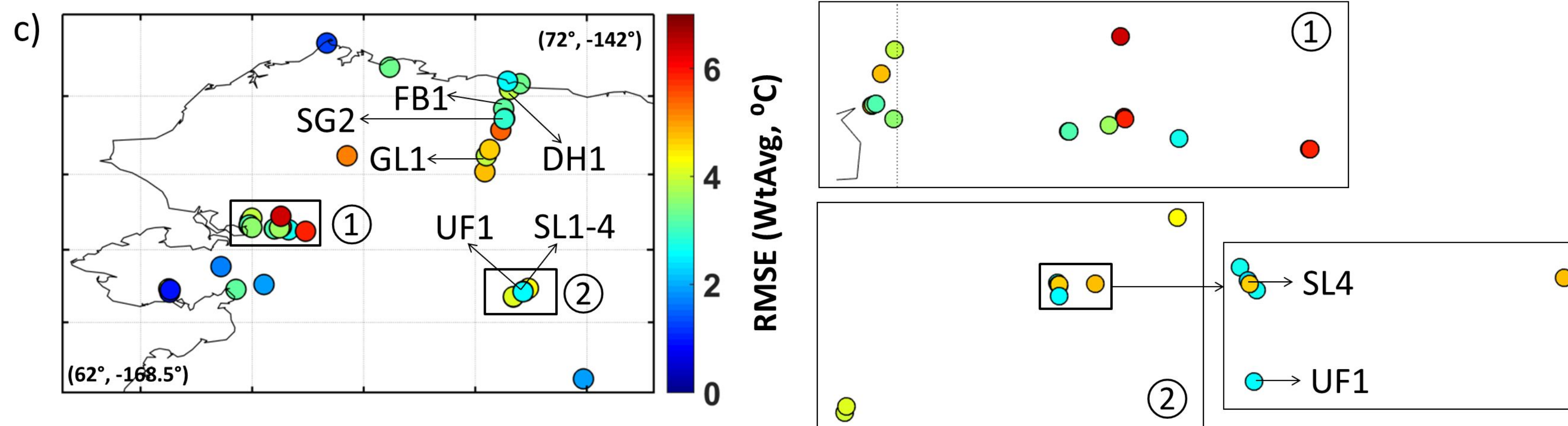
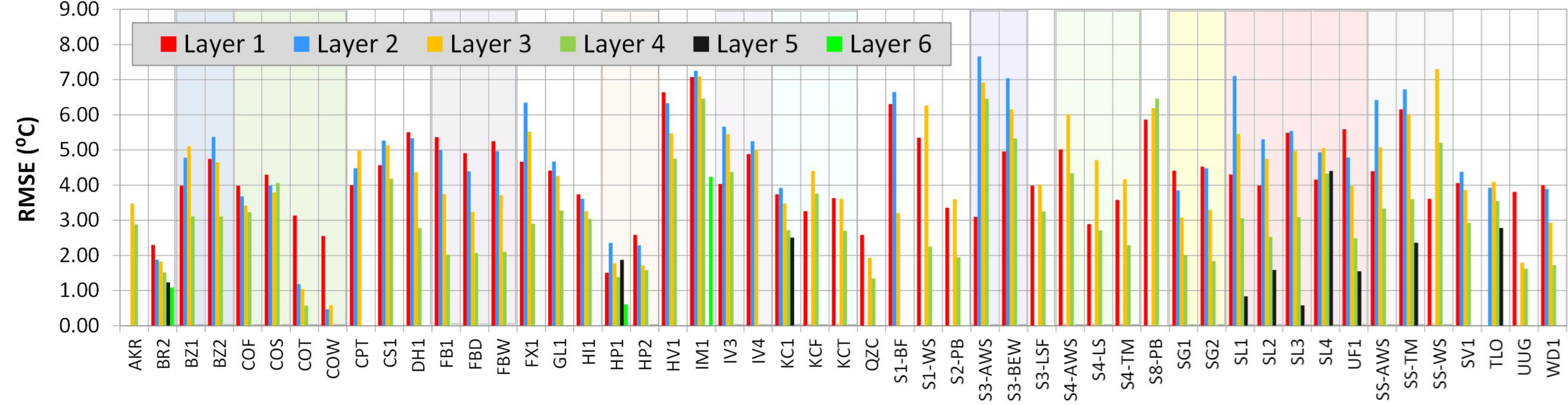
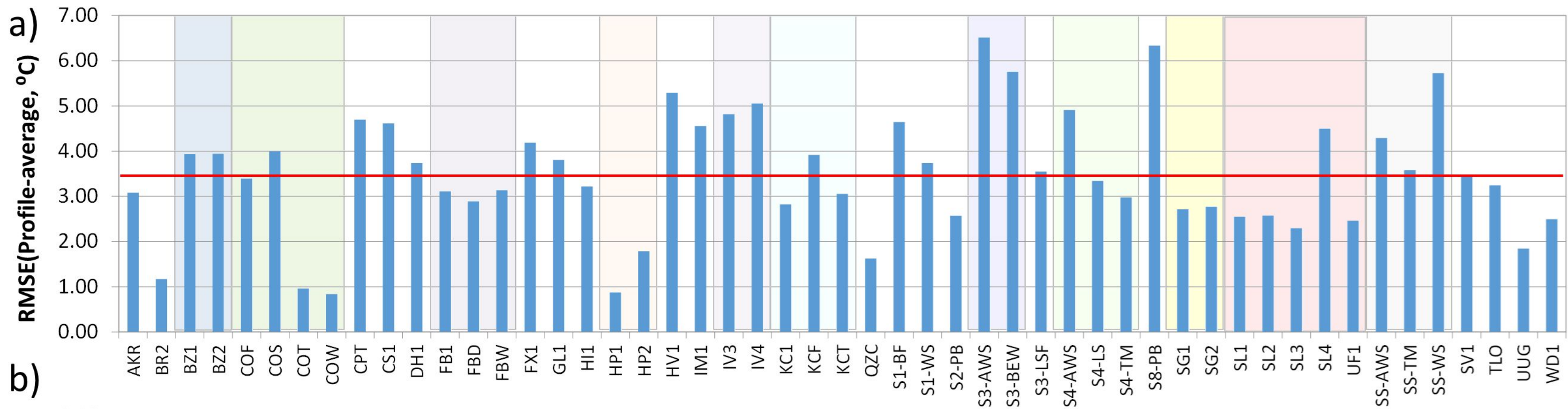
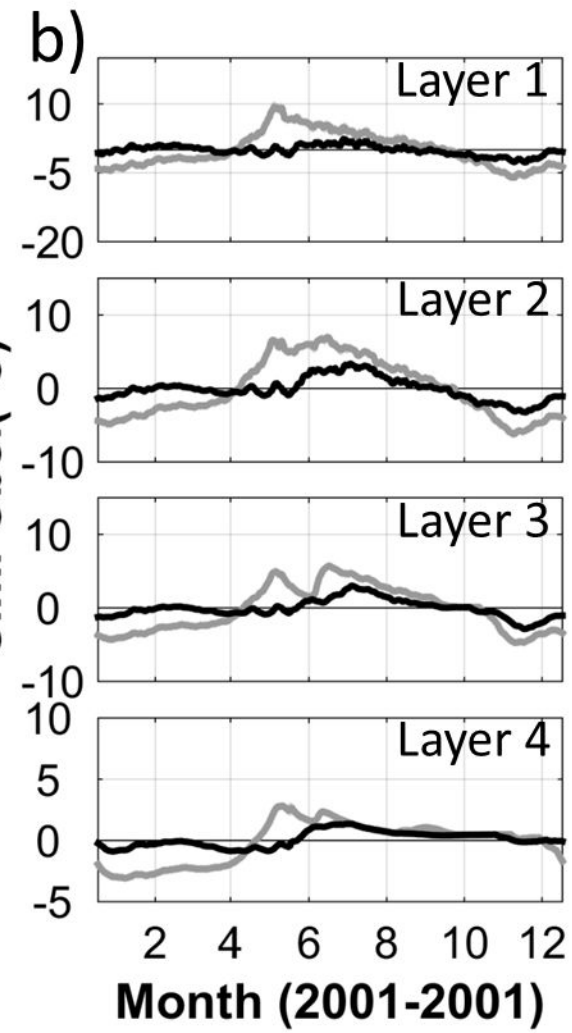
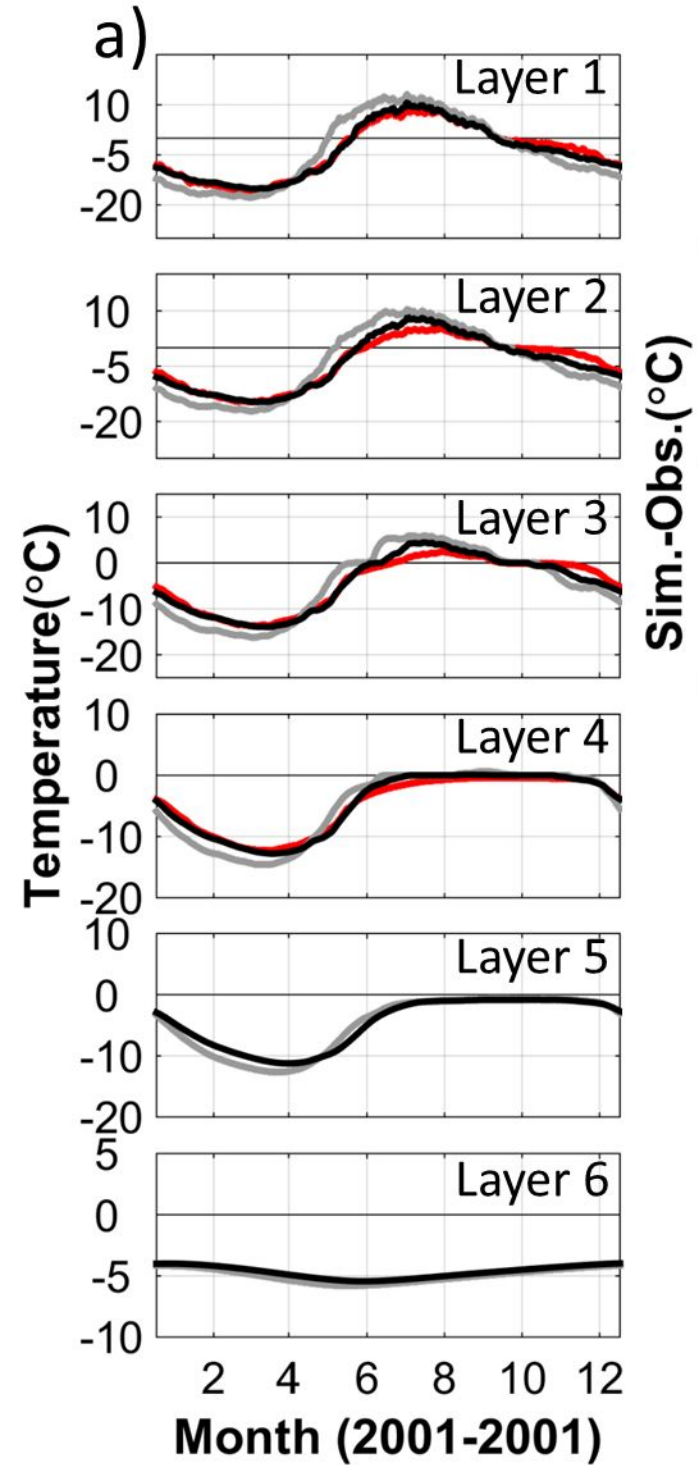


Figure 6.



— Obs.
— MERRA-2 Forcing
— Station-based Forcing

Figure 7.

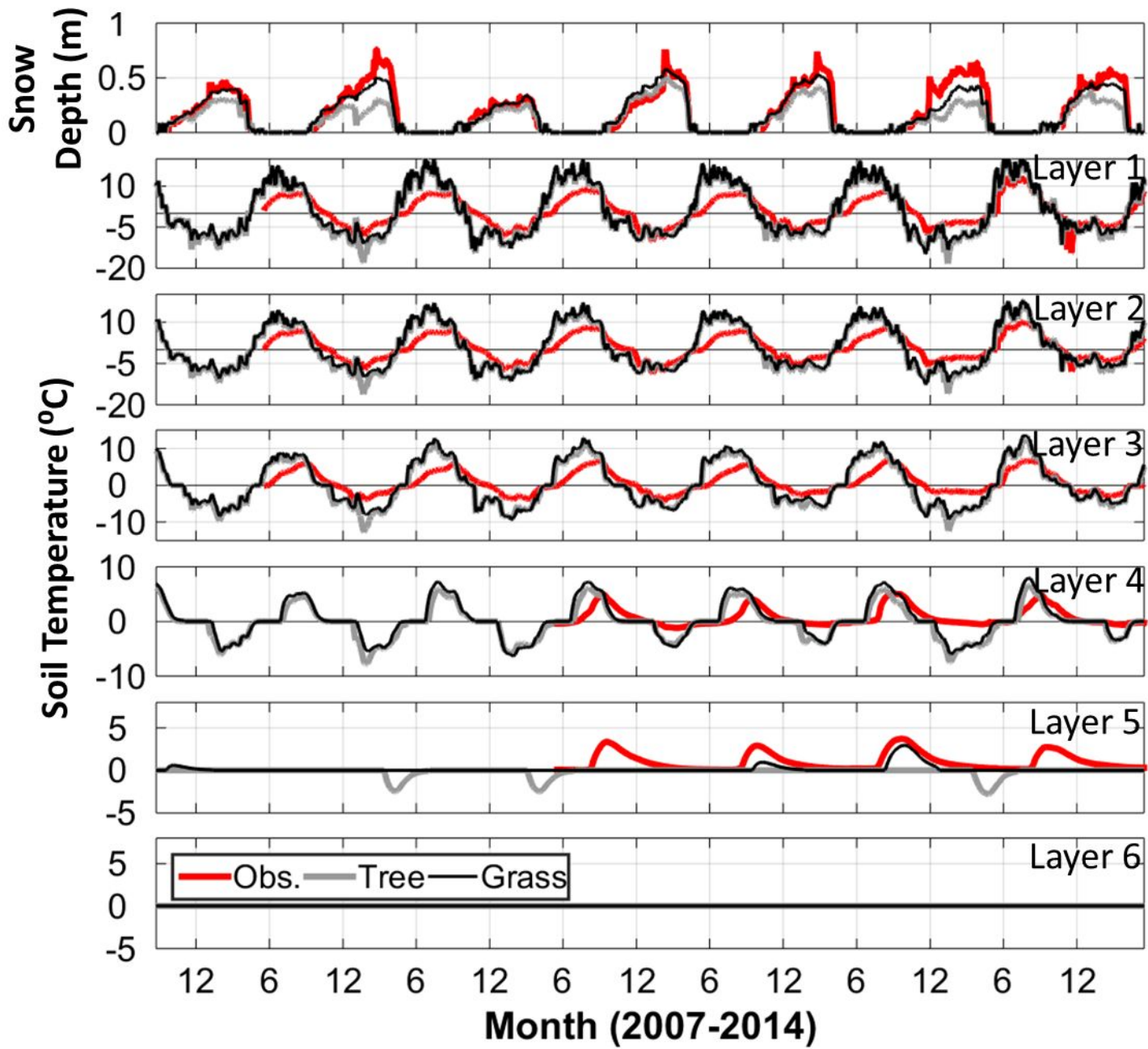
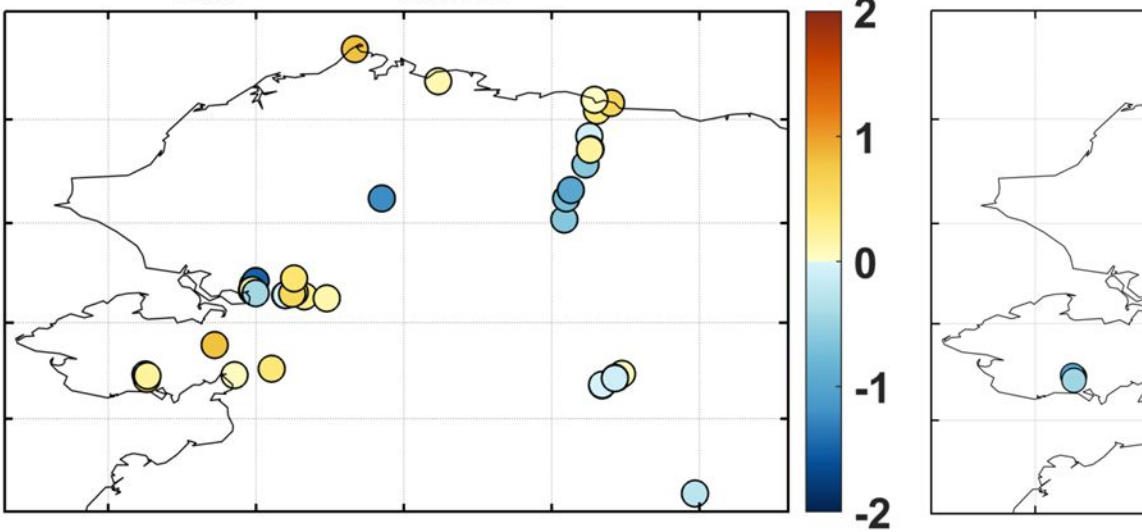
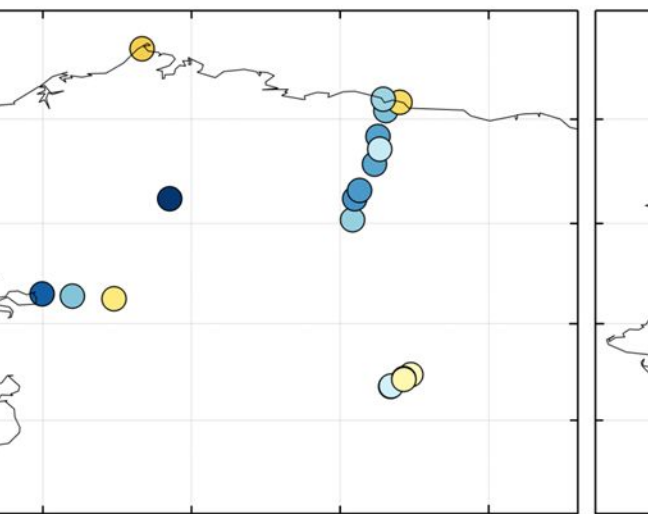


Figure 8.

a) $\text{RMSE}_{\text{Grass}} - \text{RMSE}_{\text{Baseline}} (\text{°C})$



b) $\text{RMSE}(\text{Ta0}_{\text{Grass}}) - \text{RMSE}(\text{Ta0}_{\text{Baseline}}) (\text{°C})$



c) $\text{RMSE}(\text{T01}_{\text{Grass}}) - \text{RMSE}(\text{T01}_{\text{Baseline}}) (\text{°C})$

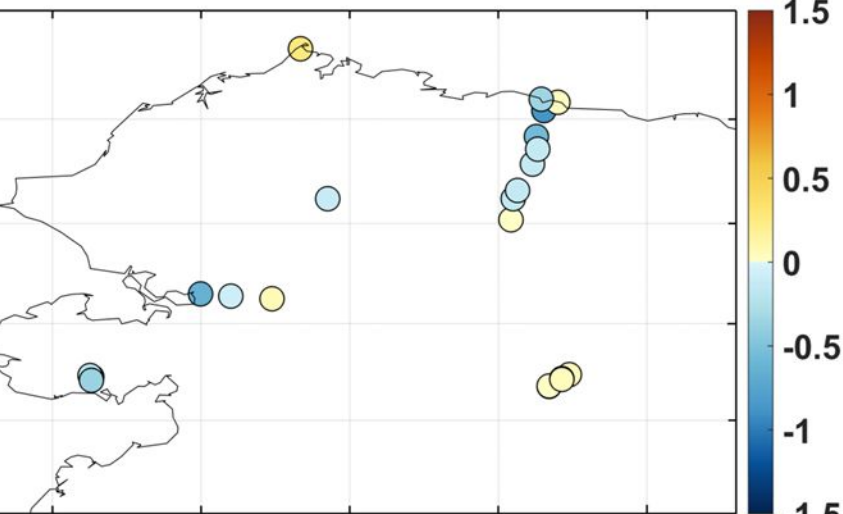


Figure 9.

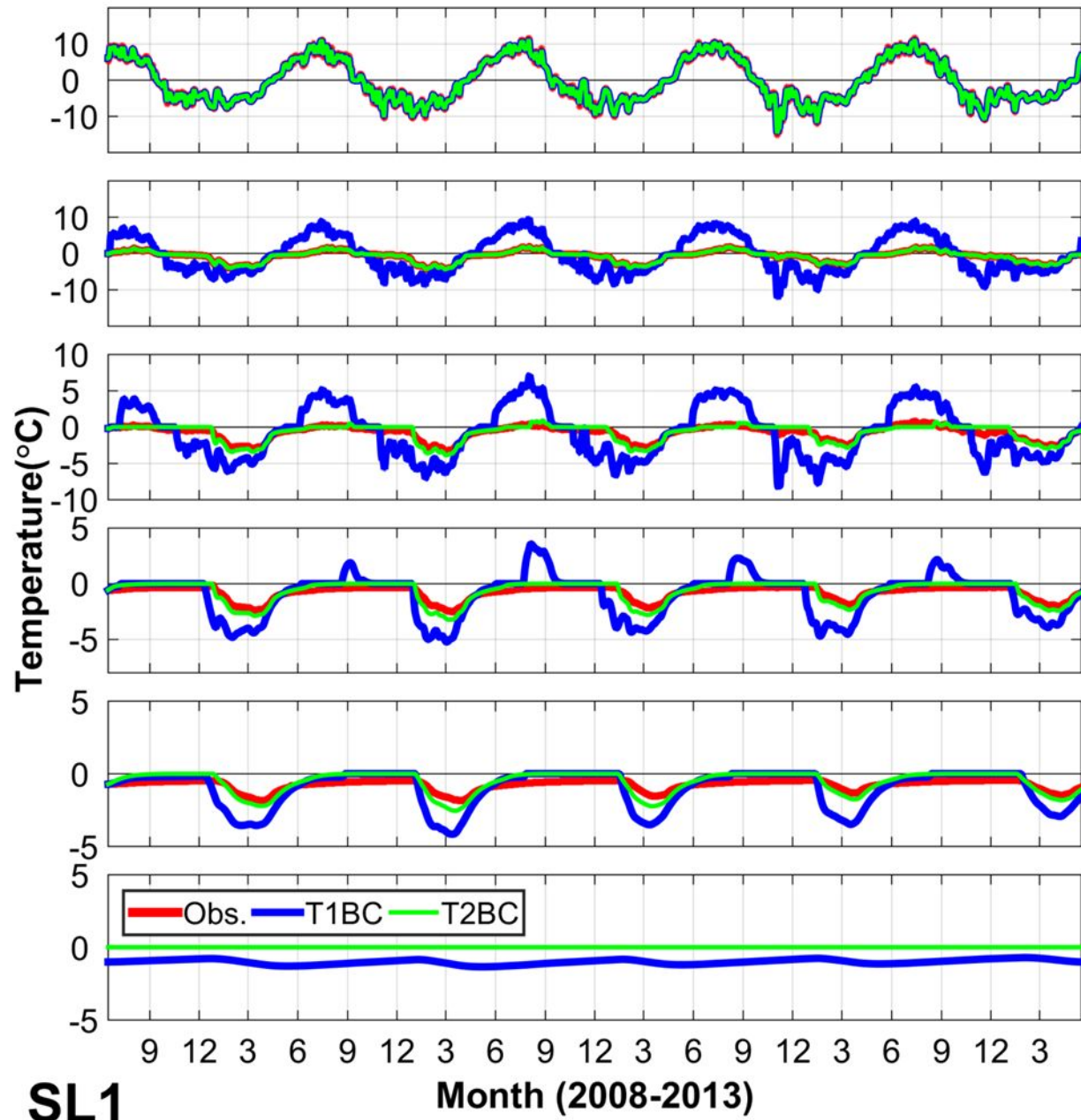
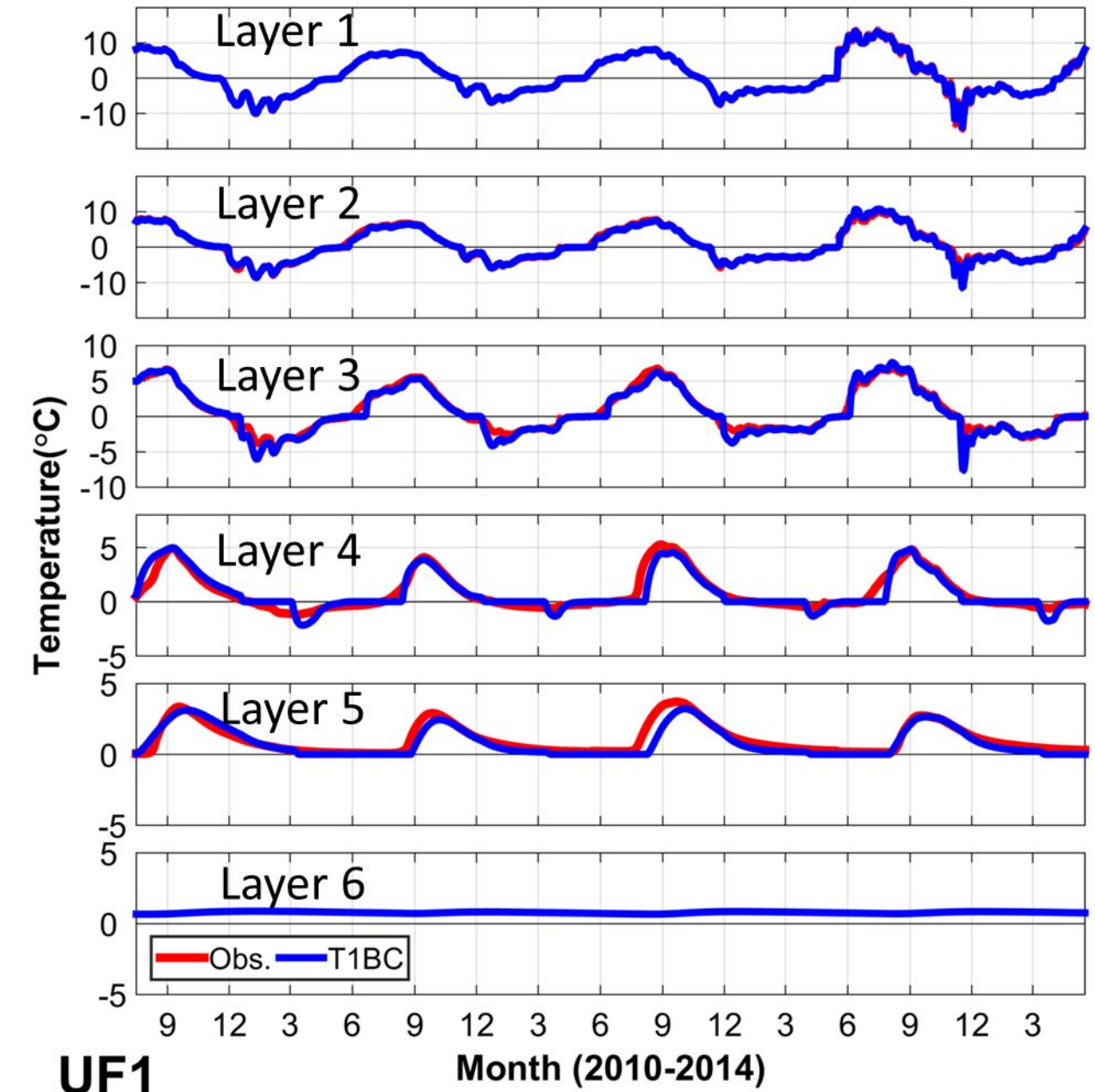
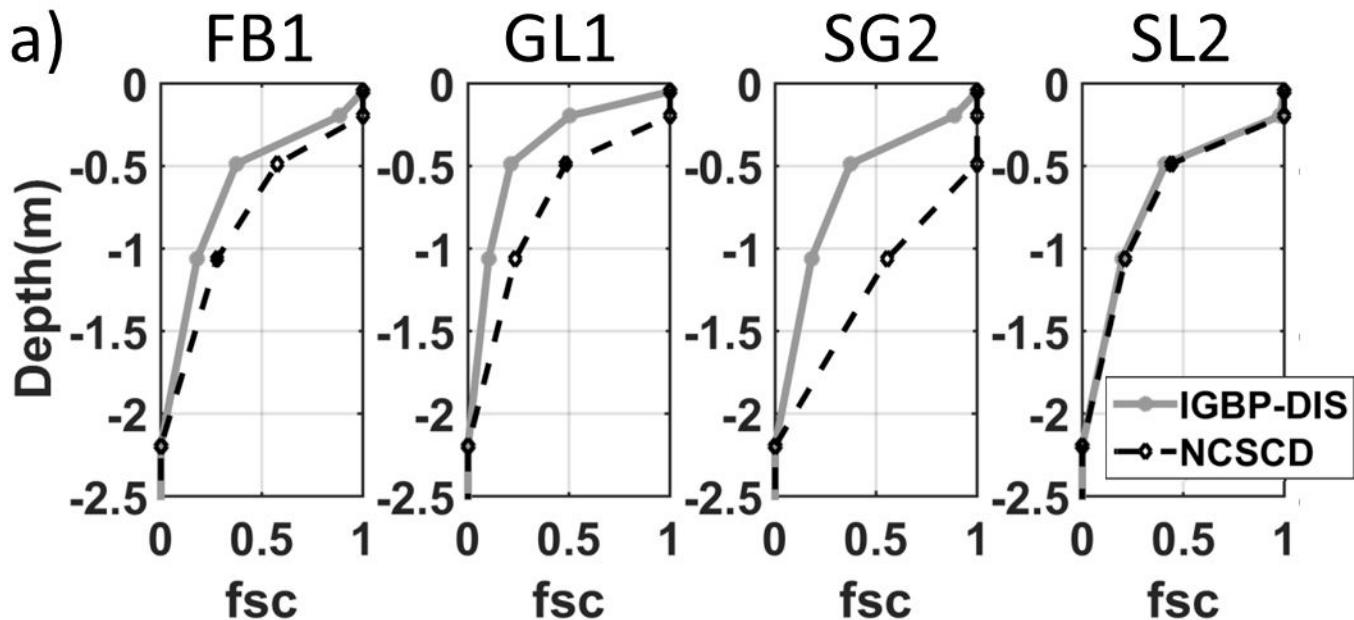


Figure 10.



b) Soil thermal properties at GL1

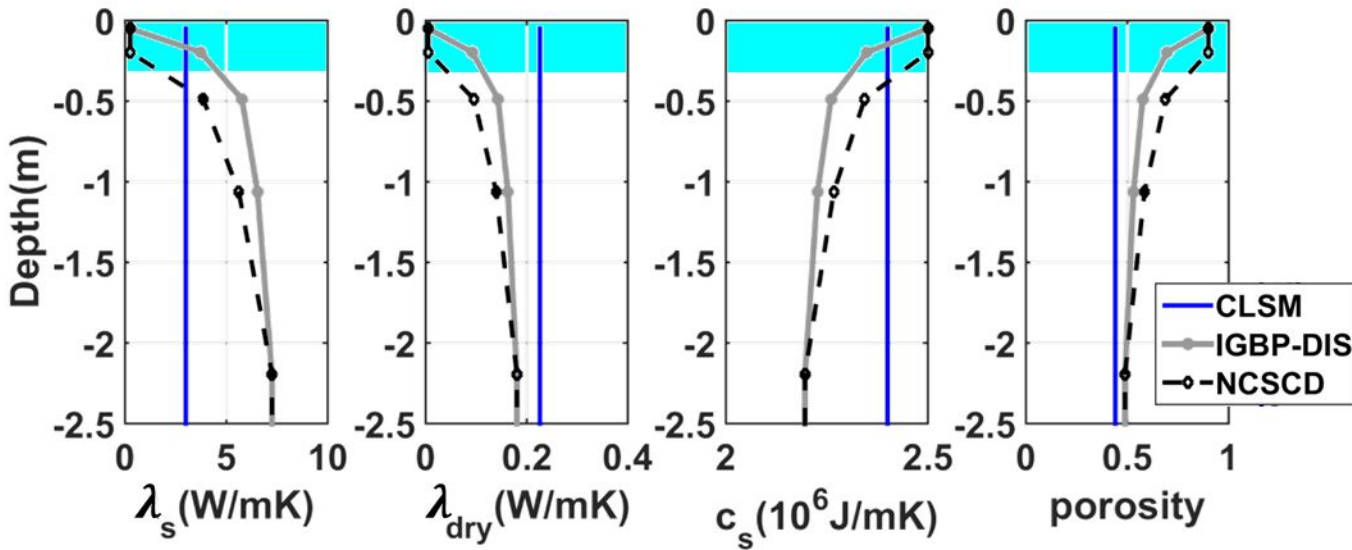


Figure 11.

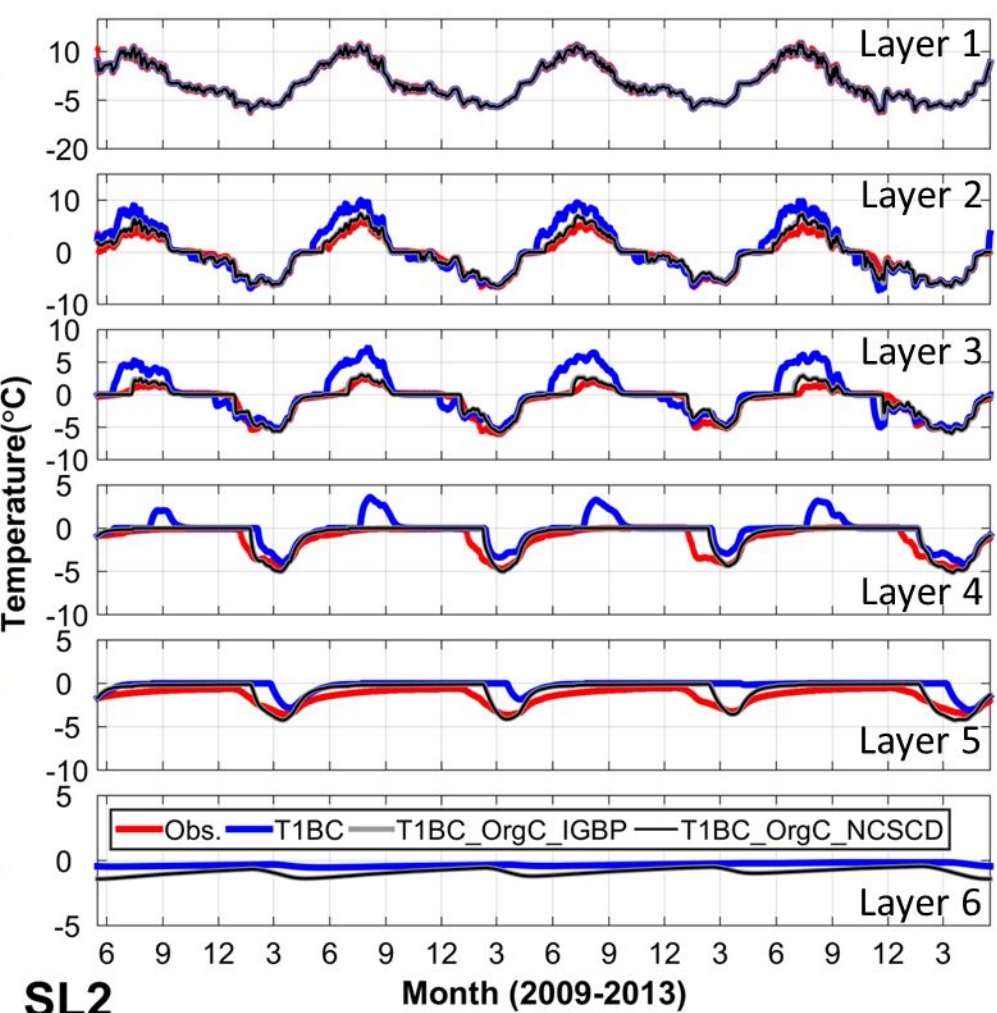
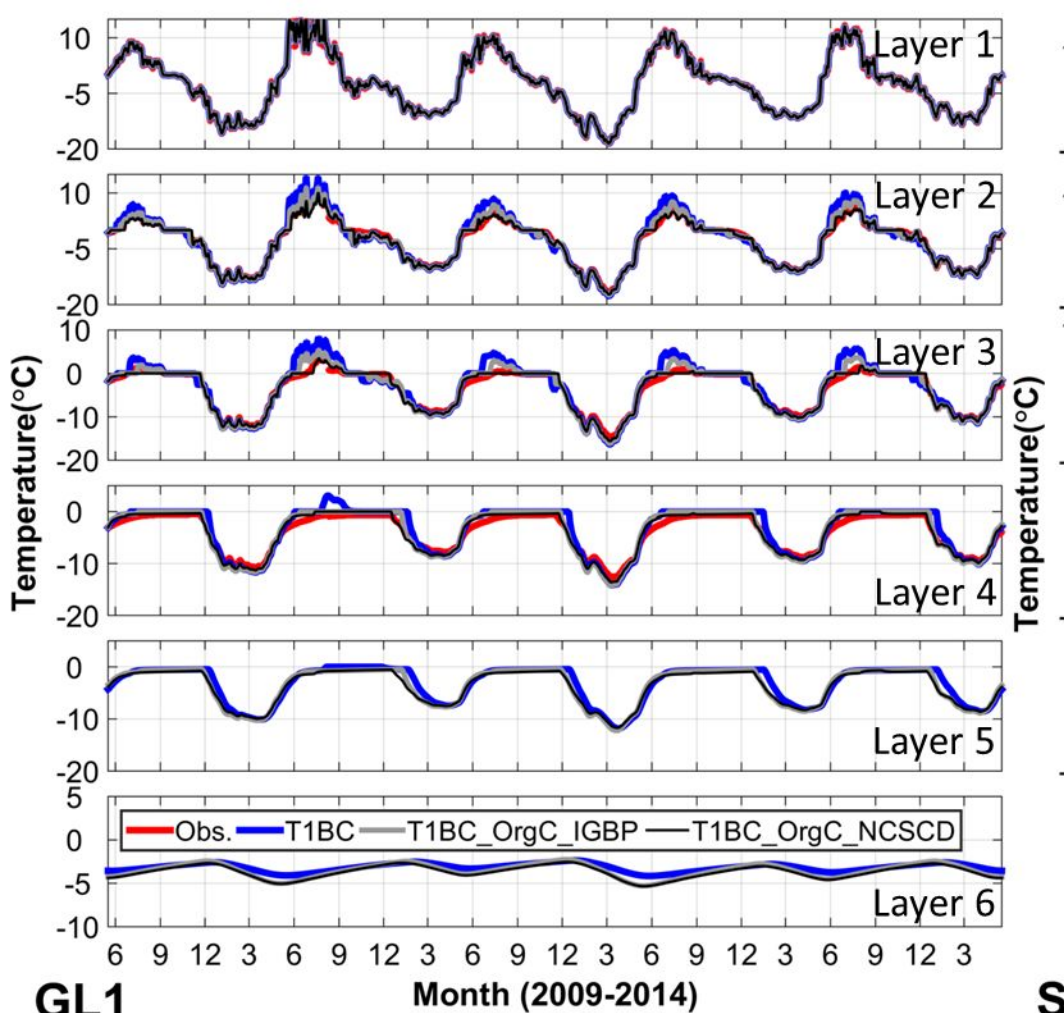


Figure 12.

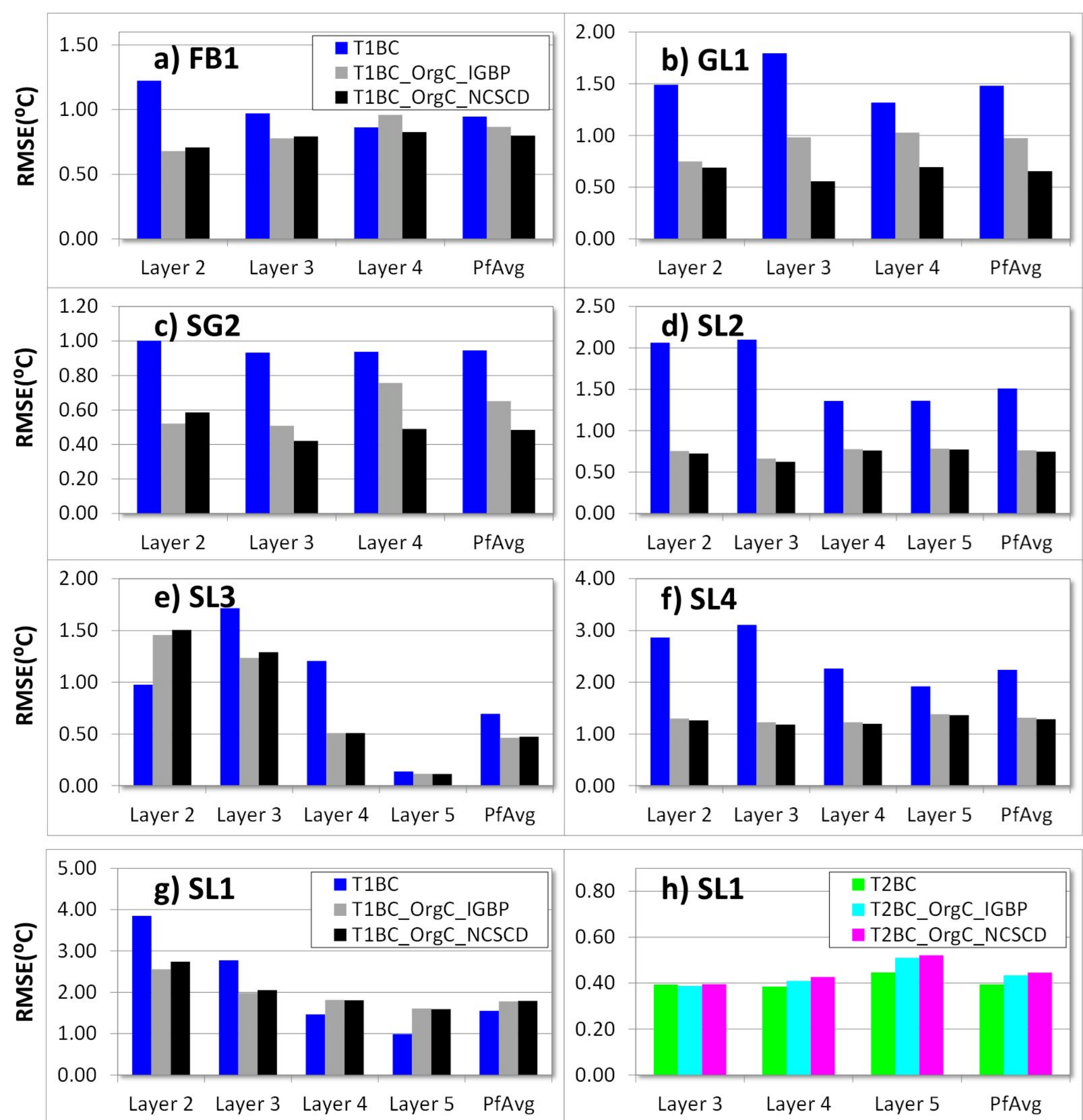


Figure 13.

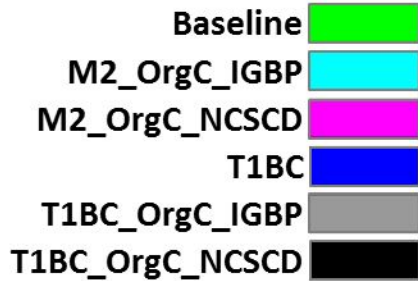
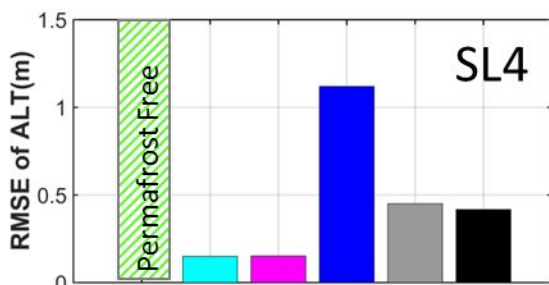
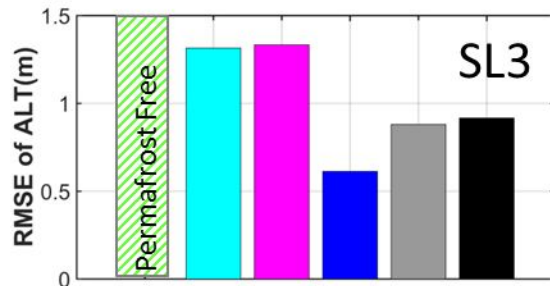
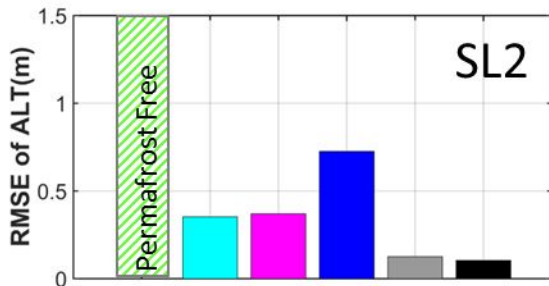
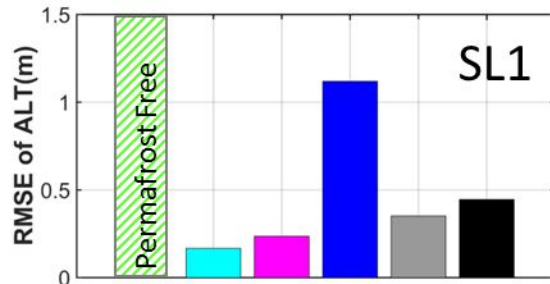
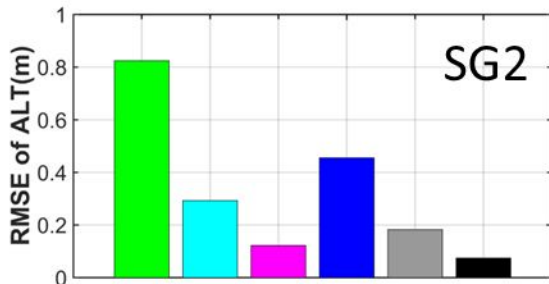
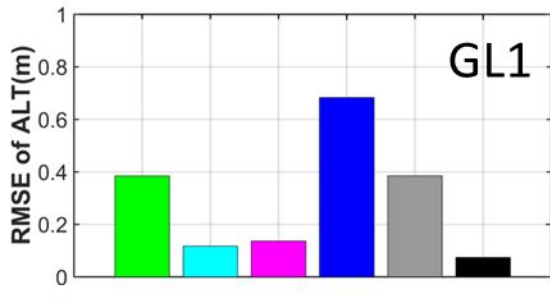
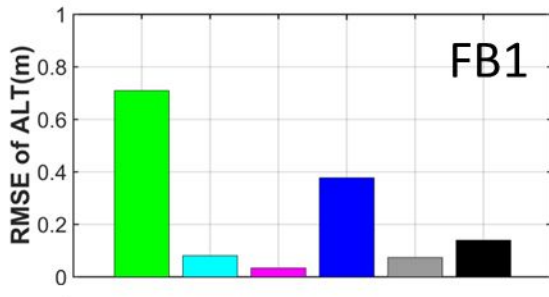


Figure 14.

